



HAL
open science

Spectroscopic autoradiography of alpha particles using a parallel ionization multiplier gaseous detector

Hugo Lefeuvre, Jérôme Donnard, Michael Descostes, Sophie Billon, Samuel Duval, Tugdual Oger, Hervé Toubon, Paul Sardini

► **To cite this version:**

Hugo Lefeuvre, Jérôme Donnard, Michael Descostes, Sophie Billon, Samuel Duval, et al.. Spectroscopic autoradiography of alpha particles using a parallel ionization multiplier gaseous detector. Nuclear Instruments and Methods in Physics Research Section A: Accelerators, Spectrometers, Detectors and Associated Equipment, 2022, 1035, pp.166807. <10.1016/j.nima.2022.166807>. <hal-04392796>

HAL Id: hal-04392796

<https://hal.science/hal-04392796v1>

Submitted on 22 Jul 2024

HAL is a multi-disciplinary open access archive for the deposit and dissemination of scientific research documents, whether they are published or not. The documents may come from teaching and research institutions in France or abroad, or from public or private research centers.

L'archive ouverte pluridisciplinaire HAL, est destinée au dépôt et à la diffusion de documents scientifiques de niveau recherche, publiés ou non, émanant des établissements d'enseignement et de recherche français ou étrangers, des laboratoires publics ou privés.



Distributed under a Creative Commons CC BY-NC 4.0 - Attribution - Non-commercial use - International License

1 **Title page**

2

3 Spectroscopic autoradiography of alpha particles using a parallel ionization multiplier gaseous
4 detector

5

6 **Coauthors:**

7 Hugo LEFEUVRE^{a, b, *}, Jérôme DONNARD^c, Michael DESCOSTES^{d, e}, Sophie BILLON^b, Samuel
8 DUVAL^c, Tugdual OGER^c, Hervé TOUBON^d, Paul SARDIN^b

9

10 **Affiliations:**

11 ^a ERM (SARL), 7 rue Albert Turpain, 86000, Poitiers, France

12 ^b IC2MP – HydrASA, Poitiers University UMR 7285 CNRS, France

13 ^c AI4R (SAS), 2 rue Alfred Kastler, Nantes, France

14 ^d ORANO Mining, R&D Dpt, 125 Av. de Paris, 92320 Châtillon, Paris, France

15 ^e Centre de Géosciences, MINES ParisTech, PSL University, 77300 Fontainebleau, France.

16

17 Corresponding author: Hugo LEFEUVRE*

18 E-mail address: hugo.lefeuvre@univ-poitiers.fr

19 Postal address: IC2MP - UMR 7285, B27, 4 RUE MICHEL BRUNET, TSA 51106 ,86073 POITIERS,
20 Cedex 9, France.

21 **Abstract:**

22 Geoscience is a field of study where nuclear instruments find their place for conducting specific
23 measurements of radioactivity, usually to improve the monitoring of natural processes using naturally-
24 occurring radioactive tracers, but also for the nuclear industry linked to the mining sector. In geological
25 samples, the location and identification of the minerals bearing radioactivity at the thin-section scale
26 remains a major challenge as the detection limit of the usual elementary microprobe techniques is far
27 higher than the concentration of most of the natural radioactive decay products. The location of each
28 decay product, as in the case of uranium-238 series in a geomaterial is interesting for relating
29 radionuclide concentrations to mineralogy. The present study aims to provide spectroscopic
30 autoradiography analysis method for measuring the initial energy of alpha particles with a parallel
31 ionization multiplier gaseous detector. This spectroscopic autoradiography method was successfully
32 used to reproduce the alpha spectra from a ²³⁸U decay chain on a geological sample at the thin-section
33 scale. The characteristics of this measurement are an energy spectrum resolution of 17.2% (FWHM) at
34 4647 keV and a spatial resolution of at least 50 μm. Even if the efficiency of energy spectrum
35 reconstruction is low (4.4%) compared to the efficiency of a simple autoradiograph (50%), this novel
36 measurement approach offers the opportunity to select areas on an autoradiograph to perform an energy
37 spectrum analysis within that area. This opens up possibilities for the detailed analysis of heterogeneous
38 geological samples containing natural alpha emitters such as uranium-238 and radium-226.

39
40
41
42

43 **Keywords:** Alpha particles; Digital autoradiography; Alpha spectroscopy; Uranium decay products;
44 Mining activities; Parallel ionization multiplier.

45

46 **1 Introduction**

47 Autoradiography [1] is a non-destructive imaging method for studying and locating in two dimensions
48 the radioactivity emanating from a surface sample, at scales ranging from hectometer to micrometer [2].
49 The distinctiveness of autoradiography is based on the fact that the source is the object itself.
50 Radioactivity imaging is performed using a detector which integrates and spatializes the radioactive
51 emissions during a given acquisition time. The image definition is closely related to the choice of sensor.
52 Film autoradiography (FA) using a silver-bromide emulsion was the first technique employed [3]. It is
53 still widely used because of its low cost and very good spatial resolution (about 10 μm). To reveal the
54 signal information, the film must be digitized. Advances in autoradiograph technology now makes it
55 possible both to digitize the activity map directly and to observe the signal accumulation in real time.
56 Autoradiography is well suited for use in the life and earth sciences. Thin sections of radiolabelled
57 animal organs mounted on microscope glass slides are conventionally imaged by autoradiography. *Ex*
58 *vivo* autoradiography is used by biologists as a complementary tool in positron emission tomography
59 (PET) [4][5], for instance to better understand drug effects or degenerative diseases. Applications of
60 autoradiography for geosciences include, among others, the characterisation of pore space and transport
61 properties of rocks [6][7][8], and the distribution of natural disintegration series in rocks [9].

62 In that context, the study of autoradiography use for alpha particle characterisation is increasing in the
63 geosciences. The present contribution is focused on the study of the natural series found in geo-materials
64 (rocks or U mill tailings). A lot of devices have been developed for imaging the emission of alpha
65 particles. The traditional method uses a solid-state nuclear track detector (SSNTD). SSNTD is a
66 medium, typically a polycarbonate film, in which the passage of an ionizing particle leaves a latent track
67 that can be made visible by an appropriate chemical treatment. Depending on the track size, the
68 observation can be performed with the naked eye, using an optical microscope or a scanning electron
69 microscope (SEM). For further details the reader can refer to applications in geosciences [10][11][12]
70 and also in biology [13]. Phosphor screens autoradiography (PSA) is an alternative method using
71 reusable films, that used to be employed for imaging the ppm of U and Th in geo-materials [14]. The
72 detection of particles is based on the property of phosphorescence. The energy imparted by incident
73 radiation (light, X-rays, gamma rays, alpha or beta particles) is temporarily stored by the excited atoms
74 in a photostimulable phosphor plate based on BaFBr: Eu^{2+} . Then, de-excitation can be induced by laser
75 scanning to stimulate characteristic emissions of photons that are interpreted to form an image. All
76 autoradiograph techniques of alpha particles described above store information in films. The sample
77 exposure time can only be estimated, so there is a high risk of overexposure or underexposure.
78 Nowadays, real-time autoradiography is becoming increasingly favored. The advantages of this
79 approach are the direct counting of the emissions, the direct digitization of the image in a raster file, and
80 the real-time acquisition. The first application of real-time autoradiographs was in the field of medicine.
81 The “ α -Camera”, used in alpha-therapy, was developed using a scintillator and a CCD camera [15][16]
82 with detector area about 5 x 5 cm^2 . The iQID system [21], which uses a similar technology to the α -

83 Camera, is described in [22]; the detector area can be 4 cm or 12.5 cm diameter. This device has
84 applications in pre-clinical and clinical scintigraphy [23]. For radiotherapy, the Timepix chip based on
85 a pixelized semi-conductor is used for alpha particle autoradiography with 14 x 14 mm² area [17][18].
86 First developed for biological applications such as alpha-therapy (using ²²³Ra) [19][20], the BeaQuant
87 system also created the first alpha autoradiograph of a geological thin section [24]. This technology is
88 based on a gaseous detector incorporating micromesh Parallel Ionization Multiplier (PIM) [25][26][27]
89 which allows the detection of both alpha and beta particles, together or separately. Alpha
90 autoradiography using this detector is considered to be not disturbed by beta particles when used in the
91 alpha imaging mode. The special feature of this autoradiograph is its large detection surface (up to 20 x
92 20 cm²) in comparison with other real-time autoradiograph. It has a good spatial resolution (<50 μm for
93 alpha and 20 μm for beta particles, mainly because the charge distribution is different), and is insensitive
94 to X-Ray and gamma. The linearity of the detector reaches five orders of magnitude. The maximal
95 acceptable counting rate over the whole analysed area is 20 × 10³ cps (counts per second), and the
96 background level for alpha counting is in the order of 6.3 × 10⁻⁴ cps/mm². The efficiency for alpha
97 particle detection is 50% according to Billon, et al., 2019 [28].

98 Concurrently, spectroscopic autoradiography (called SA) is performed by simultaneously combining
99 autoradiography with a spectral measurement. For alpha particles, different types of detector
100 technologies make this dual measurement possible. But there is often a trade-off between spatial
101 resolution, energy resolution and the field of view.

102 SSNTD can be used as a basic SA, by analysing the size distribution of the alpha tracks [29] [30]. A
103 previous study employing SSNTD demonstrated an energy resolution optimised at around 2% FWHM
104 [31] by using the range property of alpha particles. The application is however limited when alpha tracks
105 are overlaid on each other, if the activity is too high or if the exposure time is too long.

106 A scintillator coupled to a silicon photomultiplier array allows the measurement of the particles' energy
107 and emission point. For instance, in [32], the plutonium found around Fukushima has been studied by
108 spectroscopy allowing the separation of alpha and beta particles. The energy resolution was good, but
109 the spatial resolution (of 600 μm FWHM) was not suitable for high resolution autoradiography
110 applications because of the limited pixelisation (64 channels over a 26 x 26 mm² detection area).

111 As an alternative to SiPM, a demonstration using an organic scintillator (stilbene) coupled to a 8 x 8
112 position-sensitive photomultiplier tube (PS-PMT) [33] gave an energy resolution of 21.6% FWHM for
113 ²⁴¹Am.

114 Using Timepix [34] for counting and the alpha spectrometer modes to identify and quantify radon and
115 thorium gave an energy resolution of 2.3% for ²⁴¹Am (α -decay energies are 5.486 MeV). Following
116 further calibration in the alpha mode, the energy resolution is 0.7% FWHM [35][36]. However, in terms

117 of imaging, the restricted detection area of 14 x 14 mm² makes the use of this method impractical for
118 large samples. The spatial resolution can reach 18 μm [37] for alpha particles.

119 According to [38], the iQID device can locate and determine the energy of individual particles, with
120 sufficient energy resolution to distinguish between different particle types (fission fragment, β, and α
121 decay). However, using a ZnS(Ag) scintillator the expected energy resolution would not be better than
122 40% FWHM at 5.5 MeV according to reference [39][45].

123 The radiobiology application of the fluorescent nuclear track detector (FNTD) has demonstrated its
124 ability to visualise individual alpha particles and simultaneously measure their position, trajectory
125 direction and energy with good accuracy [40]. However, the detection area is limited (100 x 100 μm²)
126 and the energy resolution is 11.8% FWHM for an ²⁴¹Am source according to [41].

127 In the field of gaseous detectors, despite the possibility of having a good energy resolution [42][43],
128 there are few instruments that can combine imaging and energy measurement. For example, a 31 cm
129 thick time projection chamber using CF₄ showed an energy resolution of 6.7% (K = 1) at 5.3 MeV, and
130 a spatial resolution of 6.8 mm [44]. The latter detector has been used to measure radioactive impurities
131 of ²³⁸U and ²³²Th in low activity samples. The resolutions of different technologies are summarized in
132 Table 1.

133 In order to meet the needs of the analysis of radioactive geological samples (pluri-centimetric sample
134 and good spatial resolution), this study examines the possibility of combining the spatial and energy
135 measurement of emitted alpha particles using the BeaQuant system. Our objective is to evaluate the
136 possibility of obtaining the energy spectrum of alpha particles, with the final aim of spatializing the
137 energy distribution on the autoradiograph. This, in order to better characterize the distribution of natural
138 decay products (notably the ²³⁸U series) that can be found in geomaterials [46][47][48]. Examples for
139 ²³⁸U series are provided.

140 **2 Alpha SA method using a parallel ionization multiplier**

141 Originally, the used detector was developed and optimized for beta particle autoradiography [25].
142 Because alpha and beta particles do not interact in the same way with the detector, a simulation model
143 was performed with the Geant4 toolkit in order to understand and interpret the data measured. Alphas
144 deposit more energy than betas per unit path length and have a quasi-straight trajectory. Knowledge of
145 the particles' position and energy along their trajectory through the detector is crucial for developing a
146 spectroscopy method.

147 **2.1 Sample material and the PIM detector characteristics**

148

149 **2.1.1 Characteristics of a geological sample emission spectrum**

150 Determining the alpha emission energy spectra using the PIM is our main goal. Let E_0 be the emission
151 energy of an alpha particle when leaving the source/sample and penetrating the gas medium. E_0 is
152 influenced by the self-absorption and the loss of energy in interaction with the source media before the
153 arrival in the detector gas media. Then, the emission energy spectrum of alphas can be modified by the
154 source geometry (thickness) and nature (density). Three examples of spectra obtained with the AASI
155 simulation program [49] are shown in Supplementary Material, Figure S1. Note that a source is named
156 as “thin source” if its thickness can be neglected with respect to the mean range of the alpha particles
157 propagating into it, and “thick source” otherwise. The red spectrum corresponds to a $0.018\ \mu\text{m}$ ($9\ \text{g}/\text{cm}^3$)
158 $5485\ \text{keV}$ mono-energetic ^{241}Am alpha source. The blue one corresponds to the same emitter but in a $9\ \mu\text{m}$
159 ($9\ \text{g}/\text{cm}^3$) thick source characterized by a staircase shape falling at $5485\ \text{keV}$. The third spectrum (in
160 green), resulting from a multi-alpha $9\ \mu\text{m}$ thick source ($9\ \text{g}/\text{cm}^3$, the same as the blue spectrum),
161 illustrates the case of a “real” geological sample containing the 8 alpha emitters isotopes from the decay
162 chain of ^{238}U at secular equilibrium. One can appreciate the complexity of the spectroscopic approach
163 applied to geological samples. Indeed, they are often in the form of materials of about $30\ \mu\text{m}$ thick on a
164 thin section, and may exhibit the three natural decay chains (^{238}U , ^{235}U and ^{232}Th) in which the most
165 energetic alphas emitting from ^{214}Po ($7686\ \text{keV}$) have an average internal range of 20 to $40\ \mu\text{m}$. This
166 range combined with usual thickness of the sample means that there is considerable self-absorption and
167 energy loss.

168 **2.1.2 PIM detector description and charge readout**

169 The detector structure used for this study is schematized in Figure 1. The active part of the detector is a
170 volume of gas segmented into three zones by two thin micromeshes that are sandwiched between a
171 cathode and an anode. The cathode of the detector is the sample itself, which is mounted on a microscope
172 slide and preferably coated with a conducting layer. The gap of $400\ \mu\text{m}$ between the sample and the first
173 micromesh is achieved with a spacer machined with FR-4 material. This gap creates the first
174 amplification space (of gain G_1), placed directly in contact with the sample. The second zone of $1\ \text{cm}$
175 thickness is a drift space used to propagate the electron cloud. It is defined by the space between the two
176 micromeshes. Finally, the space between the second micromesh and the segmented anode defines the
177 third zone, which is a second amplification stage (of gain G_2).

178 An alpha particle coming from the sample interacts with the gas and generates electron-ion pairs by
179 ionization of the gas atoms along its rectilinear-like path. The number of primary electrons
180 ($\text{nb}_{\text{primary_charge}}$) is proportional to the raw energy deposited (E_{dep}) by the alpha particle in the detector.
181 The electrons created will be multiplied and collected on the segmented reading anode. The induced
182 currents generated by the charge drift in the amplification space 2 are measured by application-specific
183 integrated circuits (ASICs).

184 The intensity of the signal measured is more intense at the position where the alpha particles first ionize
185 the gas (black colour in amplification space 2, Figure 1), than the intensity measured from the
186 interactions in the drift space (dark blue in amplification space 2). The two histograms representing the
187 charge of the collected electrons (called “charge histograms”) are recorded for each event along the X
188 and Y axes. The initial position of the alpha particles, the energy deposited in the detector and the
189 projected X and Y distances of the trace are estimated thanks to these charge histograms. Unlike
190 calorimeters, since not all particles stop in the gas, the deposited energy is not directly proportional to
191 the emission energy E_0 .

192 **2.2 Simulation of the alpha emission interaction in PIM with Geant4**

193

194 **2.2.1 Behavior of alpha particles interacting with the detector**

195 The PIM detector and the alpha tracks modelled with Geant4 are shown in Figure 2. For instructive
196 purposes a point-like source having energies (E_0) uniformly distributed between 0 and 8 MeV has been
197 simulated. One can clearly notice that alpha particles show a probability of interacting with micromesh
198 1. The latter plays an important role because its geometry allows only a certain range of incidence angle
199 of alpha paths. The parameters of micromesh 1 are the diameter of the grid wire (18 μm), the distance
200 between the axes of two adjacent wires (45 μm) and the material (stainless steel). The angle of incidence
201 θ is the angle defined by the particle trajectory and the normal to the gas-sample interface. The cut-off
202 angle θ_{max} of the simulated micromesh has been estimated to 68°. The depth of the gas passed through
203 (Z coordinate) as a function of the emission energy E_0 of the alpha particle is displayed in Figure 3.

204 From the calculated 2D histogram (Figure 3, left), three types of alpha particle behaviour can be
205 distinguished with respect to the detector.

206 - *Type-1: Alphas that do not pass through micromesh 1.* If $E_0 < 40$ keV, the alpha range in
207 the gas is less than the depth of the first amplification space (400 μm); this explains why
208 particles with low emission energy never pass through micromesh 1. If E_0 ranges from 40
209 keV to 6 MeV, about 85% particles do not pass through micromesh 1. From 6 MeV onwards,
210 this proportion decreases progressively to about 63% for $E_0 = 8$ MeV. If $E_0 > 40$ keV, an
211 alpha particle deposits part of its energy in the first amplification space and may or may not
212 be stopped by micromesh 1. For example, when an alpha particle is emitted with an angle
213 of incidence $\theta > \theta_{\text{max}}$, then it is always stopped by micromesh 1. Note that the probability of
214 an alpha particle passing through micromesh 1 increases slightly with E_0 . Finally, it is
215 deduced that it is difficult to exploit type-1 alphas for spectroscopic measurements, as the
216 energy deposition in the gas is not sufficient due to the small depth of the first amplification
217 space. The fact that these alphas represent on average 80% of the total count is a factor
218 limiting the efficiency of the spectroscopic measurement.

219 - *Type-2: Calorimetric alphas.* These alphas pass through micromesh 1, but do not reach
220 micromesh 2. The deposited energy of type-2 alphas is equal to the emission energy. For 40
221 keV < E₀ < 1 MeV, the particles passing through micromesh 1 are totally calorimetrized in
222 the gas, i.e., none of them ever reach micromesh 2. For 1 MeV < E₀ < 2.7 MeV, the
223 proportion of calorimetrized alpha particles gradually decreases until it becomes zero. For
224 E₀ > 2.7 MeV, the proportion of calorimetric alpha particles is generally low. This effect is
225 due to the cut-off angle which imposes a maximum range in the gas (and consequently a
226 maximum energy of 2.7 MeV for which a particle cannot be stopped in the gas after passing
227 through micromesh 1). Nevertheless, this proportion tends to increase to about 10 % for E₀
228 = 8 MeV. This increase for high E₀ can be explained by the fact that at high energies, alpha
229 particles that interact with micromesh 1 can continue their path to be calorimetrized. These
230 events will be considered as "polluting events" for the proposed application. The type-2
231 alphas represent on average only 5% of the alphas emitted by the simulated uniform source.
232 The fact that these alphas were not used for the spectroscopy is explained below in more
233 detail.

234 - *Type-3: through-going alpha.* These are the alpha particles that have managed to pass
235 through the entire depth of the gas and end up in the anode of the detector (at the Z = 1 cm
236 coordinate). The energy deposited is therefore different from the initial energy. They
237 represent on average 15% of the events recorded. On the green curve, the proportion of the
238 crossing particles is constant and around 20% from 2.7 MeV. Around 6 MeV, there is a
239 theoretical increase in the proportion of the particles passing through with energy. These
240 alphas will be highlighted below because they exhibit a link between E₀ and the deposited
241 energy.

242 **2.2.2 From deposited energy to emission energy**

243 To exploit the energy deposited by the crossing particles, the length d of the alpha track will be used:-

$$244 \quad d = \sqrt{x^2 + y^2 + z^2} \text{ (cm)} \quad 1$$

245 where x and y are the projected distances along the X and Y axes respectively, and z the thickness of
246 the gas passed through along the Z axis. However, z is an unknown for type-2 alphas because the detector
247 does not allow us to measure this coordinate: it is not a time projection chamber. This explains why
248 type-2 alphas are not used for spectroscopy. Nevertheless, for type-3 alphas, it is possible to fix z to the
249 thickness of the detector (1 cm).

250 Knowing the deposited energy E_{dep} and the length of the track d, it is possible to relate E_{dep}/d to the
251 emission energy of the alpha particle E₀. For this, Monte Carlo simulation was used to determine the
252 distribution E_{dep}/d as a function of E₀ for all alpha particles types (Figure 4).

253 The three types of alpha events described above can be observed in Figure 4, being indicated by three
254 zones of visible colour on the right-hand distribution. Firstly, the area bordered in green corresponds to
255 the alphas that pass completely through the detector (type-3). For these alphas, the function $E_{\text{dep}}/d =$
256 $f(E_0)$ follows a bijection. The result is equivalent to the averaged Bethe curve. Secondly, the area
257 bordered in red corresponds to the calorimetrized alphas (type-2). These alphas disrupt the expected
258 bijective contribution between 1 MeV and 3 MeV. Thirdly, the alpha events in the orange-bordered area
259 are those that do not pass through micromesh 1 (type-1). The length d is greatly overestimated which
260 induces $E_{\text{dep}}/d < 200$ keV/cm for most of these events. Only those alphas that contribute to the bijective
261 distribution (type-3 alpha - selection in green) are selected; calorimetrized alphas (type-2) cannot be
262 considered for the analysis because they fall outside the bijective zone. Moreover, the type-2 alpha has
263 initial energy E_0 directly proportional to E_{dep} . But type-2 alpha cannot be used for energy measurement
264 above 2.7 MeV because their proportion is close to zero (except for “polluting events”). For application
265 to the ^{238}U series, the measurement range needs to be up to 8 MeV. The way of selecting type-3 alphas
266 is detailed in the next section.

267 **2.3 Analysis method for spectral reconstruction**

268 According to the simulation, it has been shown that among the three types of events generated, only
269 type-3 alphas can be used for reconstructing the energy spectrum (from 3 MeV to 8 MeV). The low
270 threshold of 3 MeV will be further explained in section 2.3.4. Only the alphas passing through the
271 detector can be used for a spectral reconstruction beyond 3 MeV, because in this case the length (d) of
272 the track is known and the deposited energy tends to avoid the Bragg peak at the end of the path. This
273 section describes the method for measuring the energy (E_0) spectrum of an alpha-emitting source using
274 the charge histograms.

275 **2.3.1 Particle identification**

276 The question is now to find a criterion to select type-3 alphas only. The statistical criterion used is
277 kurtosis, calculated on the charge histograms collected on the anode. The kurtosis coefficient can be
278 interpreted as a “shape feature” for charge histograms: a high value of kurtosis indicates that the
279 distribution is rather concentrated; in contrast, a low value of kurtosis describes a flat distribution.
280 Normalized kurtosis was used for the calculation (see equation 3). It is -1.2 for a continuous uniform
281 distribution, and rises to +3 for a Laplace distribution. It is 0 for a normal distribution. This coefficient
282 is useful because in most of the cases, the traversing alpha (type-3) does not deposit the "Bragg peak"
283 at the end of the path: it presents a flatter profile than the calorimetric alpha (type-2) ones. But in a few
284 cases, the peaked characteristic of the Bragg curve can be present in charge histograms for type-3 alpha.
285 Moreover, calorimetric alpha can have a charge distribution close to flat. Such a wide range of behaviour
286 makes it difficult to show a perfect discrimination between type-2 and type-3 alpha. Figure 5 (on the
287 left) gives an example of a charge histogram. The amplification "peak" is located here at position $X = 0$

288 cm while the "Bragg peak" is located at $X = -1.2$ cm. This is why it is necessary to ignore the
289 amplification peak for the calculation of kurtosis.

290 If X is a real random variable defined on an interval, then the kurtosis of X , $Kurt(X)$, is defined such
291 as:-

$$Kurt[X] = E \left[\left(\frac{X - \mu}{\sigma} \right)^4 \right] = \frac{\mu_4}{\sigma^4} \quad 2$$

292 and the normalised kurtosis is:-

$$KurtNorm[X] = Kurt[X] - 3 \quad 3$$

293

294 where E is the mathematical expectation; $\mu = E(X)$, the average of X ; μ_4 is the central moment of order
295 4; and σ , the standard deviation. Kurtosis is calculated bin by bin on the charge histograms. Figure 6
296 shows the kurtosis distribution for the three types of alpha particles. The kurtosis of the type-3 alphas
297 shows a different distribution; for example, the majority of the type-3 alphas have a kurtosis close to -
298 1.2 (green distribution, Figure 6) while type-1 and type-2 alphas exhibit a kurtosis above -1.

299 By selecting the peak related to the type-3 alphas, most of the alpha which are not usable for
300 spectroscopic measurement is eliminated. The upper boundary of the peak selection is at the interface
301 between the "pass-through" particles (green) and the calorimetrized particles (red). This interface is not
302 clearly defined as an overlap occurs between the green and red curves. However, by placing the
303 threshold at the intersection, on the abscissa there is a low percentage (3.4%) of calorimetrized particles
304 selected (against 95.8 % of pass-through alpha selected, and 0.8 % of alpha that do not pass through
305 micromesh 1). The setting of this threshold was optimized to reduce this percentage but without lowering
306 the final efficiency. An identical kurtosis calculation was also performed on the Y charge histogram.
307 Considering the charge histograms according to X and Y and using $kurt(X) < -1.1$ & $kurt(Y) < -1.1$,
308 6.4% of the events were selected from all the detected alphas used for autoradiography analysis. Once
309 the (-1.1) threshold is defined, it is a constant that does not depend on any gains which can be
310 subsequently applied to the deposited energy.

311 **2.3.2 Measurement of the energy deposited in the gas by the alpha particles**

312 The energy deposited (E_{dep}) by an alpha particle in the gas is the sum of the energy deposited in the drift
313 space and the amplification space 1. E_{dep} is calculated considering both the charge deposits along the X
314 and Y axis. Figure 5 shows a simulated charge histogram along the X axis. This is the type of data
315 provided by the PIM detector where the algorithm is applied.

316 The relationship between the deposited energy E_{dep} lost by an alpha particle to create the primary number
317 of charges measured is given by the following equation:-

$$E_{dep} = W \times nb_{Primary_charge} \quad 4$$

318 where W (eV) is the average ionisation energy (in neon gas $W = 36$ eV). The energy can be determined
 319 from the integral of the charge histogram (Figure 5, right). The energy deposited in the total gas volume
 320 of the detector along the X axis (E_{depX}) is not the integral of the entire charge histogram, but only the
 321 integral of the green area (right of Figure 5). E_{depX} can be determined using the decomposition depicted
 322 in Figure 5 (right), following equation 5:-

$$E_{depX} = E_{totalX} - E_{peakX} + E_{extrapolationX} \quad 5$$

323 where E_{totalX} is the integral of energy measured all along the track (in the drift space and amplification
 324 space 1), E_{peakX} the integral of energy in the amplification peak ($E_{peakX} = E_{1x} + E_{extrapolationX}$), and
 325 $E_{extrapolationX}$ is the energy corresponding to the mean of the primary charges created in the amplification
 326 space and multiplied by W . The same calculation is performed for determining E_{depY} for the charge
 327 histogram relates to the Y axis, E_{dep} being finally obtained by $E_{depX} + E_{depY}$. The charges related to E_{dep}
 328 measurement undergo several stages of amplification and drift, which degrades the resolution on the
 329 measured E_{dep} . The main charge peak cannot be used to determine E_0 because it corresponds to the
 330 energy deposited in the first amplification zone. This one undergoes a gain which is a function of the Z
 331 position of the charge created in the amplification space. During this process, the information on the
 332 deposited energy is thus degraded. As a consequence, the energy resolution would be insufficient using
 333 the main charge peak because the energy deduced from the main peak would be difficult to compare to
 334 E_{dep} .

335 **2.3.3 Length of ionisation tracks of particles in the gas, and selection of long tracks**

336 As stipulated previously in section 2.2.2 the calculation of track length is only possible for particles
 337 passing through the whole thickness of the detector. Nevertheless, an additional selection criterion of
 338 the tracks is necessary. Indeed, some of the preserved tracks correspond to alphas transmitted with a low
 339 angle of incidence. This implies that the deposited energy will be overlapped with the amplification
 340 peak. Moreover, a certain number of bins is necessary for the calculation of $E_{extrapolation}$. Therefore, a
 341 minimum projected track length $d_{proj} = \sqrt{dx_{min}^2 + dy_{min}^2}$ is required in order to correctly
 342 measure the deposited energy. This minimum length is set to $d_{proj} = 0.71$ cm as $dx_{min} = dy_{min} = 0.5$
 343 cm. (this length corresponding to 5 bins of the charge distribution in E_{peak} plus 8 bins to calculate
 344 $E_{extrapolation}$ and E_{dep} , where 1 bin is equal to $400 \mu m$). By applying this distance filtering in the X and Y
 345 axes, an overall theoretical efficiency of 5% is obtained for the spectral reconstruction. Note that this
 346 filtering also allows the elimination of a very large number of particles that do not pass through
 347 micromesh 1. Only 0.075% of these particles are selected by this distance filtering. Thus, the pollution
 348 from these particles is considered as negligible. To summarize, extracting E_{dep} from the charge
 349 histograms imposes a selection on d_{proj} in addition to the kurtosis criterion; these selections reduce the
 350 theoretical efficiency to 5%. This efficiency is the amount of alpha selected for the energy spectrum
 351 reconstruction divided by the amount of alpha reaching the detector and used to create the

352 autoradiograph image. By calculation, 37% of the whole type-3 alphas are selected for energy
 353 reconstruction.

354 **2.3.4 Reconstruction of the energy spectrum of the source**

355 The energy dE lost by a particle per unit length dX in a medium is defined by the linear stopping power
 356 $S = -dE/dx$ (MeV/cm). This can be described for a charged particle by the Bethe formula [50]. The
 357 stopping power depends on both the kinetic energy of the particle, and the transverse medium. The
 358 stopping power (or the mass stopping power $S.1/\rho$) is referenced on the ASTAR database [51] and
 359 plotted as a function of the kinetic energy for alpha particles in Supplementary Material, Figure S2. For
 360 the range of 2 MeV to 100 MeV the near-linearity of the log-log plot over S Energy suggests a power
 361 law relationship of the form $dE/dx = cE^d$ or reciprocally $E = a(dE/dx)^b$. For a non-relativistic particle, at
 362 moderate energies, the Bethe formula is dominated by $1/v^2$ or inversely with particle energy, suggesting
 363 $b = 1$. However, it represents only a theoretical approximation; furthermore, the Bethe formula breaks
 364 down at very low energy. So, the power function with “b” and “a” as parameters will be used in this
 365 section as a fitting function to establish the relationship between E_{dep}/d and E_0 .

366 In addition, a gaseous detector needs amplification in order to have enough charge collected to detect a
 367 signal above the electronic noise. So, the energy deposited in the gas (E_{dep}) can be defined as an initial
 368 energy deposited in the gas (E_{dep_ini}) multiplied by a gain G_2 created by the amplification space 2:-

$$E_{dep} = G_2 \times E_{dep_ini} \quad 6$$

369 The emission energy E_0 of the particle is calculated as a function of the energy deposited in the gas (E_{dep})
 370 and the length of the track (d) by applying a power function (equation 7), which corresponds to the fit
 371 of the bijection linking E_{dep}/d and E_0 obtained on the type-3 alpha (see above Figure 4):-

$$E_0 \left(\frac{E_{dep}}{d} \right) = a \times \left(\frac{E_{dep}}{d} \right)^b \quad 7$$

372 For any gain G_2 , the power law for the calibration function can be written as equation 8:-

$$E_0 \left(\frac{E_{dep}}{d} \right) = a \times \left(\frac{G_2 \cdot E_{dep_int}}{d} \right)^b \quad 8$$

373 For a detector without gain (i.e. $G_2 = 1$), there is a new function with new coefficient a' and b' defined
 374 in equation 9.

$$E_0' \left(\frac{E_{dep_ini}}{d} \right) = a' \times \left(\frac{E_{dep_int}}{d} \right)^{b'} \quad 9$$

375 There is an equality with energy measurement $E_0 = E_0'$, which means that (8) = (9). Theoretically, b
 376 must depend only on the physical parameters of the detector, mainly the density and the gas composition.
 377 That results in the calculation of G_2 in equation 10:

$$\begin{cases} b = b' \\ G_2 = \left(\frac{a'}{a}\right)^{\frac{1}{b}} \end{cases}$$

378 In order to simplify the simulation, the choice was made to fix $G_2 = 1$. In this case E_{dep} is equal to $E_{\text{dep_ini}}$
 379 and the coefficients become $b = b' = b_{\text{sim}}$, and $a = a' = a_{\text{sim}}$.

380 Figure 7 illustrates the relationship between the energy deposited by the particles in the gas per unit
 381 length (E_{dep}/d) and the initial energy of the particles (E_0) more precisely. The parameters a_{sim} and
 382 b_{sim} of this power law are determined by adjustment (see red curve Figure 7). The fit gives $a_{\text{sim}} =$
 383 20183600 and $b_{\text{sim}} = -1.26$.

384 This distribution has been drawn without plotting the alpha that interact with micromesh 1 and lose part
 385 of their energy inside it. The effect of those alpha is visible on Figure 8 where $E_{0_reconstructed}$, a
 386 function of $E_{0_initial}$, should follow a linear function if the spectral reconstruction succeeds. For 74.5 %
 387 of alpha, it is the case. But for 24 % the initial energy is modified. This modification is not an error of
 388 reconstruction because it is intrinsically due to interaction between the alpha and micromesh 1 (alpha
 389 can be of type-2 or -3). However, the selected alpha with $E_0 < 1.5$ MeV (1.5 %) do not follow the power
 390 reconstruction function precisely. Those effects are visible in the final energy spectrum reconstruction
 391 on Figure 9.

392 Figure 9 (left) gives the initial energy spectrum E_0 obtained with the algorithm described in this section,
 393 which would have been a uniform spectrum between 0 MeV and 8 MeV. The corresponding efficiency
 394 Figure 9 (right) is the number of alpha selected in the spectrum with original energy E_0 , divided by the
 395 number of alpha generated by the source at E_0 energy.

396 Firstly, on the reconstructed spectrum, an under-count of around 8 MeV is observed, caused by the effect
 397 of energy resolution. Secondly, between 2 and 3 MeV, an over-count is observed, caused by: (1)
 398 calorimetric particles which are not filtered by the kurtosis criterion (with $E_0 < 1.5$ MeV) and which are
 399 reconstructed as higher energy they have; and (2) alphas which lose energy because of micromesh 1.
 400 Thirdly, another effect is visible on the reconstructed spectrum. It looks as if the spectrum decreases
 401 slightly from 4 to 8 MeV which is contradictory to the efficiency curve. This does not stem from the
 402 efficiency of the detection method. Such behaviour is inherited from the selected alpha which interact
 403 and lose energy inside micromesh 1 and change the final distribution of reconstructed energy.

404 As a consequence, the range of the spectrum lower than 3 MeV has not been used because of the over-
 405 count in that range. The maximum energy studied is 8 MeV (this is a limitation coming from ^{238}U series).
 406 The valid measurement ranges from 3 to 8 MeV. In this case, the mean efficiency is defined by the
 407 number of alpha falling inside this energy range [3-8 MeV] divided by the total number of alpha
 408 detected, and has a value of 3.9 %.

409 The Geant4 simulation used in this section has its own limitations. For instance, thermodynamics
410 phenomena (variations of temperature and pressure) are not considered, as well as electronic noise
411 associated to the ASIC reading. Moreover, electric fields, recombination phenomena and grid
412 transparency are not considered. The electron drift speed is not taken into account in the proposed
413 simulations ($V_d_{\text{electron}} = 5 \text{ cm}/\mu\text{s}$), which may induce shifts in the charge measurement between the
414 beginning and end of the track. No physical simulation of the gain G_2 in the second amplification space
415 (this gain is considered as unitary) has been performed. Some parameters of the simulation are defined
416 after experimental feedback, such as the amplification gain in the first space. The proposed simulation
417 is however sufficient to obtain data and spectra comparable to those measured by the PIM detector. By
418 analysing these data, a methodology is established here that enables the measurement of an energy
419 spectrum of an alpha particle source.

420 **3 Results**

421 The previous section described a method to theoretically measure an energy spectrum for alpha particles.
422 In order to apply this method to real samples it is important to develop a calibration method. A calibrated
423 sample with multiple radionuclides was used.

424 **3.1 Thin source of ^{226}Ra used for calibration**

425 The calibration source described (named ^{226}Ra source) is a disk (NucFilm DiscTM) composed of a thin
426 layer of manganese dioxide containing radium-226. This source covers a polyamide support of 24 mm
427 diameter. The ^{226}Ra is trapped in a 20 mm diameter area. The ^{226}Ra decays and emits an emission energy
428 spectrum which is assimilated to that of a thin source including the ^{226}Ra and its decay products
429 (Supplementary Material, table S1).

430 In Figure 10 the spectrum of the ^{226}Ra source was measured using an alpha spectrometer CANBERRA
431 model 7401, coupled with a passivated implanted planar silicon (PIPS) detector for alpha spectroscopy
432 (A450-18AM, 450 mm², 18 keV FWHM at 5.486 MeV). The ^{226}Ra activity is higher than for its
433 daughters. For an acquisition time of 28811 s (~8h), the recorded counting rate is 0.28 cps for an energy
434 spectrum ranging from 1 to 8 MeV. The alpha spectrum is not that of a perfectly fine source, but it
435 comes close. For the presented application, this source is nevertheless considered as a fine source
436 because the width of the observed peaks is well below the energy resolution of the used device.

437 The measurement was conducted using a large area sample holder (12 x 8 cm²) with the BeaQuant,
438 using Alpha-mode, with the ^{226}Ra source in the center of the sample holder. This sample holder was a
439 little different from the configuration used in the simulation. In this case, the source needed to be placed
440 on another micromesh. Each contact between this micromesh and the source reduced the number of
441 alpha detected, and introduced an optical transparency of 51%. But this new component did not change
442 the methodology used for the energy measurement. The autoradiograph representing the spatial
443 distribution of the radioactivity on the source surface is shown in Figure 11.

444 To determine the a and b parameters of equation 7, it was necessary to use a calibration source during
 445 each acquisition. This source had to contain two sufficiently distinct energy peaks E_{cal1} and E_{cal2} ,
 446 separated by at least 2 MeV, in a range between 3.5 and 8 MeV; the ^{226}Ra source with its daughters was
 447 then used as a calibration source. Its emission spectrum contains the main ^{226}Ra peak at 4784 keV and
 448 the ^{214}Po peak at 7686 keV. In this sample, the system of two equations with two unknowns to be solved
 449 is the following (equation 11):-

$$\begin{cases} a \times x_1^b = E_{cal1} \\ a \times x_2^b = E_{cal2} \end{cases} \quad 11$$

450 where x_1 and x_2 are the values of E_{dep}/d associated respectively with $E_{cal1} = 4670$ keV and $E_{cal2} = 7392$
 451 keV. These values are calculated by fitting the degraded alpha energy spectrum of Figure 10, to take the
 452 detector energy resolution into account. This degraded alpha energy spectrum is obtained by convolving
 453 the spectrum on Figure 10 by a normal law of fixed standard deviation ($\sigma = 342$ keV). Because the
 454 energy resolution is “worth” more than the energy resolution of the spectrum on Figure 10, the two
 455 energy peaks E_{cal1} and E_{cal2} do not correspond to the peaks defined above. An average of energy around
 456 the two peaks results from this degradation, which is however very close to their theoretical values.
 457 Moreover, the corresponding theoretical energy is also shifted by the sample thickness.

458 The expression of a and b is deduced by equation 12:-

$$\begin{cases} b = \frac{\ln\left(\frac{E_{cal1}}{E_{cal2}}\right)}{\ln\left(\frac{x_1}{x_2}\right)} \\ a = \sqrt{E_{cal1} * E_{cal2}} * e^{-b \ln(\sqrt{x_1 x_2})} \end{cases} \quad 12$$

459 To determine the variables X_1 and X_2 , a fitting of the E_{dep}/d distribution (Figure 12) is performed using
 460 two Gaussian functions. These histograms were built after selecting particles passing through the
 461 detector according to the method described in Section 2.3. The values of X_1 and X_2 correspond to the
 462 expectation of each normal distribution. In the example of the ^{226}Ra source studied, $X_1 = 22220$
 463 channels/cm and $X_2 = 15686$ channels/cm.

464 The calibrated values of the coefficients calculated using equation 12 are $b = -1.31$ and $a = 2422661904$.
 465 It can be seen that a and b are different from the simulation (a_{sim} and b_{sim}), and this shows the need
 466 for a calibration.

467 Finally, the energy E_0 is measured particle by particle with the power law defined with the parameters a
 468 and b calculated previously. Figure 13 shows the spectrum reconstructed with this power law. The
 469 spectrum is plotted on Figure 13 (in red) and superimposed on the alpha spectrum obtained with alpha
 470 spectrometry after degradation. It is consistent with the spectrum of the source measured by alpha
 471 spectrometry and confirmed the hypothesis that the proportion of ^{226}Ra has remained constant over time.
 472 The energy resolution of the PIM detector can also be deduced from these results. It is measured at 7.3

473 % (K = 1) or 17.2% FWHM at 4647 keV by fitting the corresponding peak with a normal distribution.
 474 The corresponding reconstruction efficiency is 5.4 % between 3 and 8 MeV.
 475 The coefficient “a” depends on the gain G_2 corresponding to the second amplification space. This gain
 476 G_2 is a constant multiplication factor applied to E_{dep} for all alpha events and can vary from one
 477 acquisition to another. The method to determinate the coefficient “a” (or indirectly G_2) is described in
 478 the next section.

479

480 **3.2 Calibration optimisation when the gain G_2 is variable**

481 It can be seen that the “a” coefficient from the calibration method is far higher than from the simulation
 482 “a_sim”. Such a result is in agreement with the expression of the “a” coefficient, including the gain G_2 .
 483 Equation 13 gives the relation linking G_2 and “a” coefficient:-

$$\begin{cases} b = b' \\ a = \frac{a'}{G_2^b} \end{cases} \quad 13$$

484 where a' and b' are coefficients from a real acquisition using gain $G_2 = 1$, and a and b are coefficients
 485 from a real acquisition with any gain G_2 (because $b < 0$ and $G_2 > 0$ then $a > a'$).

486 It can be seen that G_2 is easier to introduce because it gives a physical sense to the “a” coefficient. G_2
 487 can be determined thanks to the calibration process described hereafter.

488 Concurrently, the coefficients a' and b' cannot be determined experimentally because if we set $G_2 = 1$
 489 with the electronics, there will not be enough charge collected by the detector to go above the threshold
 490 charge detection. However, the modelling described in Section 2.3 was achieved with $G_2 = 1$ ($E_{dep} =$
 491 E_{dep_int}). So, it is possible to fix the coefficient by $a' = a_sim$. Another issue is that $b' = b \neq b_sim$. So, if
 492 a_sim is used, the results of G_2 will not be the realistic value of the gain, but a relative value (because
 493 a_sim is an approximation of a'):-

$$G_2 = \left(\frac{a_sim}{a} \right)^{\frac{1}{b}} \quad 14$$

494 According to this method the value of G_2 can be estimated with equation 14. With the calibration source
 495 a calculated value is $G_{2_cal} = 38.16$.

496 Now, the calibration processes can be optimized in order to calibrate “any” sample by calculating the
 497 “a” coefficient. For that, the coefficient $b = -1.31$ is fixed by the calibration method thanks to the ^{226}Ra
 498 source. Then, the coefficient $a' = a_sim = 20183600$ is also fixed. Finally, G_2 is calculated when the
 499 difference ϵ (defined in equation 15) between the spectroscopy chain alpha spectrum distribution after
 500 degradation ($S1_i$) and the spectrum distribution ($S2_i$) is a minimum. G_2 can be “adjusted” (so “a” also
 501 changes). ϵ is plotted in Figure 14 for different value of G_2 .

$$\varepsilon(G_2) = \sqrt{\sum_{i=1}^n (S1_i - S2_i(G_2))^2}$$

502 By applying this minimization of error technique, a corresponding $G_2 = 38.15$ was determined when ε
 503 is at its minimum. G_2 is nearly identical to $G_{2,cal}$ with the first calibration process. With this technique,
 504 any sample can be calibrated if the alpha spectrum determined by alpha spectrometry is known.

505 **3.3 Application using a geological sample**

506 In order to test and validate the energy spectrum reconstruction method, an acquisition of a thick
 507 geological sample exhibiting ^{238}U and its decay products at secular equilibrium was achieved. The
 508 results are described hereafter.

509 The source is a uranium ore from Congo (rock age 600 My), containing uraninite (UO_2), and showing
 510 some localized uranotile and coffinite alterations. It was prepared at Bessines sur Gartempe (France)
 511 and comes from the historical collection of Orano Mining (sample 9689-03). The sample is in the form
 512 of a 7 mm-thick uraninite "piece" placed in a resin and polished on its surface. The emission energy
 513 spectrum of this source was measured with an alpha spectrometer CANBERRA model 7401 (Figure
 514 15), over an acquisition time of 9671 s (~ 2.5 h). The measured counting rate is 83.7 cps between 3000
 515 keV and 8000 keV.

516 The sample is considered as a multi-alpha thick source. The measured spectrum corresponds to the
 517 superposition of eight energy steps coming from the eight alpha emitters of the ^{238}U natural decay chain
 518 (Supplementary Material, table S2). The source is at secular equilibrium, so that all isotopes from the
 519 decay chain demonstrate the same alpha activity. In the ^{238}U series, 2.5 My are approximately necessary
 520 to reach secular equilibrium (corresponding to about ten periods of ^{234}U).

521 The autoradiograph image shown in Figure 16 (right) was performed with the large area sample holder
 522 in order to be under the same conditions as the calibration source presented above in Alpha-mode. The
 523 surface activity measured is 418 cps (or 0.9 cps/mm²). The acquisition time used for measuring a
 524 spectrum on the whole section is 7239 s.

525 The spectrum of the ^{238}U sample is measured by applying the spectral reconstruction method. This
 526 spectrum is shown in red in Figure 17, and it was adjusted using the calibration method described in
 527 section 3.2, with the error ε minimization. During this calibration, the spectrum taken as a reference for
 528 the calculation of error is the one from Figure 15 which has been degraded by normal function
 529 convolution (shown in blue on Figure 17). The calibration leads to the calculation of gain $G_2 = 36.90$.
 530 The spectrum matches the alpha spectroscopy chain. The counting rate recorded in the range of [3-9]
 531 MeV is 18.7 cps. So, the efficiency of the spectrum reconstruction is 4.4 % in this energy range, and the
 532 PIM detector has 22.3 % of the efficiency of the alpha spectrometer described above. The superposition

533 region around 3 MeV is still visible. A slight decrease in efficiency at 4.5 MeV is also observed. Overall,
534 the two spectra in Figure 17 are very similar.

535 The results mean that the PIM detector can both measure the position of alpha particles and measure
536 their energy. The efficiency of the developed spectroscopic technique is globally low. This can be a
537 detection limit for some applications if the sample activity is low. The acquisition time can also be
538 adjusted to compensate with this low efficiency. For example, considering that 2000 entries in the energy
539 spectrum are sufficient for interpretation, this corresponds to a count rate of 0.075 cps for one week of
540 acquisition time. In terms of uranium content, and considering a 1 mm² region of interest, this count rate
541 is related to about 3 wt% of uranium in secular equilibrium. If the application of the spectral modality
542 seems feasible for multi-source, it needs to be tested more deeply for heterogeneous geological samples.

543 **4 Conclusion**

544 The described energy spectrum measurement method is based on an algorithm applied to data of an ideal
545 point source representing the interaction of alpha particles with a PIM detector, whose elements were
546 geometrically optimized. The spectral reconstruction efficiency is 4.4%, and the energy resolution is
547 poor compared to a semiconductor (but is still better than other technologies). In addition, the efficiency
548 can surely be improved by using a sample holder in exactly the same configuration as shown in Figure
549 1, and also by optimising the algorithm of energy reconstruction. However, these results already make
550 it viable to use spectroscopic autoradiography on geological samples. This measurement will allow the
551 study of the spatial distribution of uranium and its descendants in geo-materials by coupling SEM
552 characterizations. For this purpose, a complementary complex radioactive source material modelling
553 could be considered. The direct application of this dual modality (energy-position) of analysis will be
554 the subject of future developments. The measurement of the radioactive equilibrium state of
555 heterogeneous geological structures, and the quantitative mapping of ²²⁶Ra radioactivity are now being
556 actively studied.

557 **Supplementary material**

558 **Acknowledgements**

559 This work has been done within the framework of a CIFRE Ph. D thesis (n°2020/0166) convention
560 between the University of Poitiers, ERM (SARL) (Poitiers, France) and ANRT. We would like to thank
561 Marc Brouand (ORANO Mining company) for the samples preparation. We would like to thank Julie
562 Champion from Subatech Laboratory for her valuable assistance during the spectroscopy measuring
563 campaign.

564 **References**

565 [1] F. Bourrel, P. Courrière, Radionucléides - Application : biologie moléculaire, Techniques de
566 l'Ingénieur, V1 (2003) 3362 - 3363.

- 567 [2] P. Fichet et al., Tritium analysis in building dismantling process using digital autoradiography,
568 Journal of Radioanalytical and Nuclear Chemistry, 291 (2012) 869 - 875.
- 569 [3] G.A. Boyd, Autoradiography in Biology and Medicine, Academic Press, 1955.
- 570 [4] A. Biegon, C. Mathis, W. Jagust, Autoradiography as a Tool for PET/SPECT Tracer Selection
571 and Assessment, Academic Press, (1996) 26 - 33.
- 572 [5] O. Alitalo et al., Digital autoradiography for efficient functional imaging without anesthesia in
573 experimental animals: Reversing phencyclidine-induced functional alterations using clozapine,
574 Progress in Neuro-Psychopharmacology & Biological Psychiatry, 100 (2020) 109887.
- 575 [6] E. Muuri et al., Electronic autoradiography of ^{133}Ba particle emissions; diffusion profiles in
576 granitic rocks, Applied Radiation and Isotopes, 149 (2019) 108 - 113.
- 577 [7] N. Macé, P. Fichet et al., Use of quantitative digital autoradiography technique to investigate
578 the chlorine-36-labelled radiotracer transport in concrete, Applied Geochemistry, 100 (2019)
579 326 - 334.
- 580 [8] M. Voutilainen et al., Characterization of spatial porosity and mineral distribution of crystalline
581 rock using X-ray micro computed tomography, C-14-PMMA autoradiography and scanning
582 electron microscopy, Applied Geochemistry, 101 (2019) 50 - 61.
- 583 [9] G. Devès et al., Chemical element imaging for speleothem geochemistry: Application to a
584 uranium-bearing corallite with aragonite diagenesis to opal (Eastern Siberia, Russia), Chemical
585 Geology, 294–295 (2012) 190 - 202.
- 586 [10] S.M. Zhmodik et al., The study of distribution and forms of uranium occurrences in Lake Baikal
587 sediments by the SSNTD method, Radiation Measurements, 40 (2005) 532 - 538.
- 588 [11] A.A. Ochmann, A.T. Solecki, CR-39 autoradiographic micromapping of rock sections of
589 various alpha emitters content – calibration approach, Journal of Environmental Radioactivity,
590 79 (2005) 127 - 136.
- 591 [12] T. Pi et al., Autoradiography of geological fluorite samples for determination of uranium and
592 thorium distribution using nuclear track methodology, Sociedad Mexicana de Física, 53 (2007)
593 57 - 60.
- 594 [13] S. Kodaira et al., Evidence of Local Concentration of α -Particles from ^{211}At -Labeled Antibodies
595 in Liver Metastasis Tissue, Journal of Nuclear Medicine, 60 (2019) 497 - 501.
- 596 [14] J.M. Cole et al., Phosphor imaging as a tool for in situ mapping of ppm levels of uranium and
597 thorium in rocks and minerals, Chemical Geology, 193 (2013) 127 - 136.
- 598 [15] T. Bäck, L. Jacobsson, The α -Camera: A Quantitative Digital Autoradiography Technique
599 Using a Charge-Coupled Device for Ex Vivo High-Resolution Bioimaging of α -Particles,
600 Journal of Nuclear Medicine, 51 (2010) 1616 - 1623.
- 601 [16] N. Chouin et al., Ex Vivo Activity Quantification in Micrometastases at the Cellular Scale Using
602 the α -Camera Technique, Journal of Nuclear Medicine, 54 (2013) 1347 - 1353.

- 603 [17] R. AL Darwish et al., Autoradiography Imaging in Targeted Alpha Therapy with Timepix
604 Detector, Computational and Mathematical Methods in Medicine, (2015) e612580.
- 605 [18] C. Teyssier et al., Exploitation of the charge sharing effect in Timepix device to achieve sub-
606 pixel resolution in imaging applications with alpha particles, Astroparticle, Particle, Space
607 Physics and Detectors for Physics Applications, 7 (2012) 681 - 687.
- 608 [19] N. Benabdallah et al., Radium-223 Treated Primary Patient Bone Biopsy Analysis: Macro to
609 Microscale Analyses and Dosimetry, Journal of Nuclear Medicine, 61 (2020) 531.
- 610 [20] N. Benabdallah, Optimisation de la dosimétrie en alphathérapie par approche multi-échelle :
611 application au traitement des métastases osseuses par le ^{223}Ra , PhD manuscript, Université
612 Paris-Saclay, (2017).
- 613 [21] B.W. Miller, Radiation Imagers for Quantitative, Single-particle Digital Autoradiography of
614 Alpha- and Beta-particle Emitters, Seminars in Nuclear Medicine, 48 (2018) 367 - 376.
- 615 [22] B.W. Miller et al., Quantitative single-particle digital autoradiography with α -particle emitters
616 for targeted radionuclide therapy using the iQID camera, Medical Physics, 42 (2015) 4094 -
617 4105.
- 618 [23] L. Han, B.W. Miller, et al., Applications of iQID cameras, Proceedings SPIE Volume 10393,
619 Radiation Detectors in Medicine, Industry, and National Security XVIII, (2017) 165 - 170.
- 620 [24] P. Sardini et al., Quantitative autoradiography of alpha particle emission in geo-materials using
621 the Beaver™ system, Nuclear Instruments and Methods in Physics Research Section A:
622 Accelerators, Spectrometers, Detectors and Associated Equipment, 833 (2016) 15 - 22.
- 623 [25] J. Donnard et al., Advancements of labelled radio-pharmaceutics imaging with the PIM-MPGD,
624 Journal of Instrumentation, 4 (2009) P11022.
- 625 [26] J. Donnard et al., The micro-pattern gas detector PIM: A multi-modality solution for novel
626 investigations in functional imaging, Nuclear Instruments and Methods in Physics Research
627 Section A: Accelerators, Spectrometers, Detectors and Associated Equipment, 610 (2009) 158
628 - 160.
- 629 [27] J. Donnard et al., High Spatial Resolution in β -Imaging with a PIM Device, IEEE Transactions
630 on Nuclear Science, 56 (2009) 197 - 200.
- 631 [28] S. Billon, P. Sardini et al., From Bq cm^{-3} to Bq cm^{-2} (and conversely) – Part 1: a useful
632 conversion for autoradiography. Journal of Radioanalytical and Nuclear Chemistry, 320 (2019)
633 643 - 654.
- 634 [29] S.M.H. Pooya et al., Passive α -particles spectrometry by polycarbonate SSNTD using new
635 etching conditions, Radiation Physics and Chemistry, 77 (2008) 949 - 953.
- 636 [30] M.F. Zaki, Y.H El-Shaer, Particularization of alpha contamination using CR-39 track detectors,
637 PRAMANA journal physic, 69 (2007) 567 - 574.
- 638 [31] O.A. Bondarenko et al., performance of alpha particle spectroscopy using a TASTRAK™
639 detector, Radiation Measurements, 26 (1996) 59 - 64.

- 640 [32] Y. Morishita et al., Detection of alpha particle emitters originating from nuclear fuel inside
641 reactor building of Fukushima Daiichi Nuclear Power Plant, *Scientific Reports*, 9 (2019) 581.
- 642 [33] Y. Morishita, Development of an alpha- and beta-imaging detector using a thin-stilbene plate
643 for radon-222 progeny measurements, *Radiation Measurements*, 140 (2021) 106511.
- 644 [34] M. Janik et al., Optimization of the Timepix chip to measurement of radon, thoron and their
645 progenies, *Applied Radiation and Isotopes*, 107 (2016) 220 - 224.
- 646 [35] M. Holik et al., Alpha calibration of the Timepix pixel detector exploiting energy information
647 gained from a common electrode signal, *Journal of Instrumentation*, 14 (2019) C06022.
- 648 [36] C. Granja et al., Resolving power of pixel detector Timepix for wide-range electron, proton and
649 ion detection, *Nuclear Instruments and Methods in Physics Research Section A: Accelerators,
650 Spectrometers, Detectors and Associated Equipment*, 908 (2018) 60 - 71.
- 651 [37] J. Vallergera et al., High-resolution UV, alpha and neutron imaging with the Timepix CMOS
652 readout, *Nuclear Instruments and Methods in Physics Research Section A: Accelerators,
653 Spectrometers, Detectors and Associated Equipment*, 591 (2018) 151 - 154.
- 654 [38] B.W. Miller et al., The iQID camera: An ionizing-radiation quantum imaging detector, *Nuclear
655 Instruments and Methods in Physics Research Section A: Accelerators, Spectrometers,
656 Detectors and Associated Equipment*, 767 (2014) 146 - 152.
- 657 [39] Y. Morishita et al., Performance comparison of scintillators for alpha particle detectors, *Nuclear
658 Instruments and Methods in Physics Research Section A: Accelerators, Spectrometers,
659 Detectors and Associated Equipment*, 764 (2014) 383 - 386.
- 660 [40] J.J.M. Kouwenberg et al., Alpha radiation dosimetry using Fluorescent Nuclear Track Detectors
661 *Radiation Measurements*, 113 (2018) 25 - 32.
- 662 [41] J.A. Bartz et al., An imaging spectrometer based on high resolution microscopy of fluorescent
663 aluminum oxide crystal detectors, *Radiation Measurements*, 56 (2013) 273 - 276.
- 664 [42] N. Hasebe et al., α -particle spectrometer based on xenon gas ionization chamber using coplanar
665 electrodes, *Nuclear Inst. and Methods in Physics Research Section A: Accelerators,
666 Spectrometers, Detectors and Associated Equipment*, 925 (2019) 123 - 127.
- 667 [43] K. Iwasaki et al., Development of Gas Ionization Chambers with Coplanar Electrodes for Alpha-
668 ray Spectrometry, *Proceedings of International Symposium on Radiation Detectors and Their
669 Uses, JPS Conf. Proc*, 11, 010003 (2016).
- 670 [44] H. Ito et al., Development of an alpha-particle imaging detector based on a low radioactivity
671 micro-time-projection chamber, *Nuclear Instruments and Methods in Physics Research Section
672 A: Accelerators, Spectrometers, Detectors and Associated Equipment*, 953 (2020) 163050.
- 673 [45] Y. Morishita et al., Flexible alpha camera for detecting plutonium contamination, *Radiation
674 Measurements*, 103 (2017) 33 - 38.

- 675 [46] A. Angileri et al., Mapping ^{238}U decay chain equilibrium state in thin sections of geo-materials
676 by digital autoradiography and microprobe analysis, *Applied Radiation and Isotopes*, 140
677 (2018) 228 - 237.
- 678 [47] S. Billon et al., Quantitative imaging of ^{226}Ra ultratrace distribution using digital
679 autoradiography: Case of doped celestines, *Journal of Environmental Radioactivity*, 217 (2020)
680 106211.
- 681 [48] J-F. Moyen et al., Multi-scale spatial distribution of K, Th and U in an Archaean potassic
682 granite: a case study from the Heerenveen batholith, Barberton Granite-Greenstone Terrain,
683 South Africa, *South African Journal of Geology*, 124, (2021) 53 - 86.
- 684 [49] T. Siiskonen, R. Pöllänen, Advanced simulation code for alpha spectrometry, *Nuclear*
685 *Instruments and Methods in Physics Research Section A*, 550 (2005) 425 - 434.
- 686 [50] G.F. Knoll, *Radiation Detection and Measurement*, 3rd ed., John Wiley & Sons, New York,
687 2000, p 31.
- 688 [51] ASTAR, available at <https://physics.nist.gov/PhysRefData/Star/Text/ASTAR.html>, (accessed
689 on January 1st, 2022).

Figure 1: Principle of the PIM detector. An alpha particle is coming from the sample, and interacts with the gas within the chamber of the detector.

Figure 2: Alpha track visualization with Geant4 in the (X, Z) plane close to micromesh 1. The alpha source is a point source. Micromesh 1 is simulated by a set of bars parallel to the X and Y axes, the bars parallel to the Y axis in the (X, Y) plane are visible. The z distance between the source and micromesh 1 is 400 μm .

Figure 3: Left: 2D histogram showing the depth of gas passed (Z in cm) as function of the alpha emission energy E_0 . Right: Proportion of the three identifiable alpha event types as a function of E_0 .

Figure 4: Bethe curves ($E_{\text{dep}}/d = f(E_0)$) obtained using Geant4 simulations, for all types of alphas. Left: using $d = \sqrt{x^2 + y^2 + z^2}$, which cannot be experimentally measured; Right: using $d = \sqrt{x^2 + y^2 + 1}$ which can be estimated using the PIM. The orange, red and green selections correspond to alpha types 1, 2 and 3, respectively.

Figure 5: Left: Boundaries used in charge histogram (in X here) for the calculation of kurtosis (for type-2 alpha event example). Right: schematic illustration of the total energy calculation.

Figure 6: Kurtosis distribution for the three alpha types; type-1 in blue; type-2 in red; type-3 in green.

Figure 7: Distribution of E_0 according to E_{dep}/d , obtained for particles sorted by kurtosis and projected distance criteria (Bethe curve). The distribution is adjusted by a power law (in red).

Figure 8: Distribution of E_0 reconstructed versus E_0 initial when the particle leaves the source.

Figure 9: Left: Reconstructed spectrum, obtained from a uniform activity source; Right: efficiency of the reconstruction method.

Figure 10: Energy spectrum of the ^{226}Ra source obtained with an alpha spectrometry chain (acquisition made in 2017).

Figure 11: alpha autoradiograph of the ^{226}Ra source obtained with the autoradiograph. A surface counting rate of 0.32 cps was measured.

Figure 12: Distribution of E_{dep}/d for selected alpha particles of ^{226}Ra calibration sample.

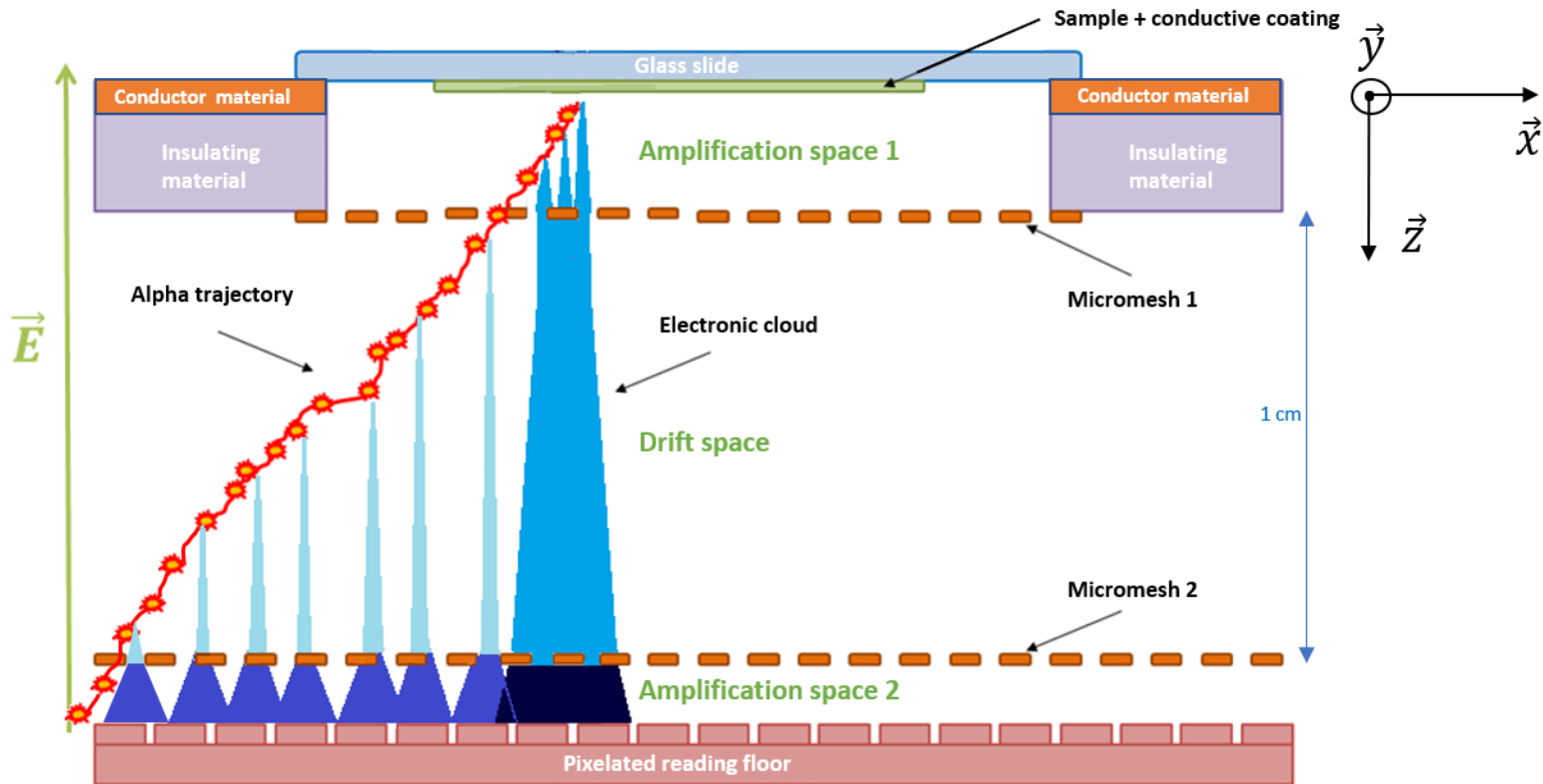
Figure 13: Comparison of the spectrum (divided by their respective internals) of the calibration source (^{226}Ra) obtained experimentally with the PIM detector and SA method (red) with the spectrum obtained from the spectroscopy chain, after degradation (blue).

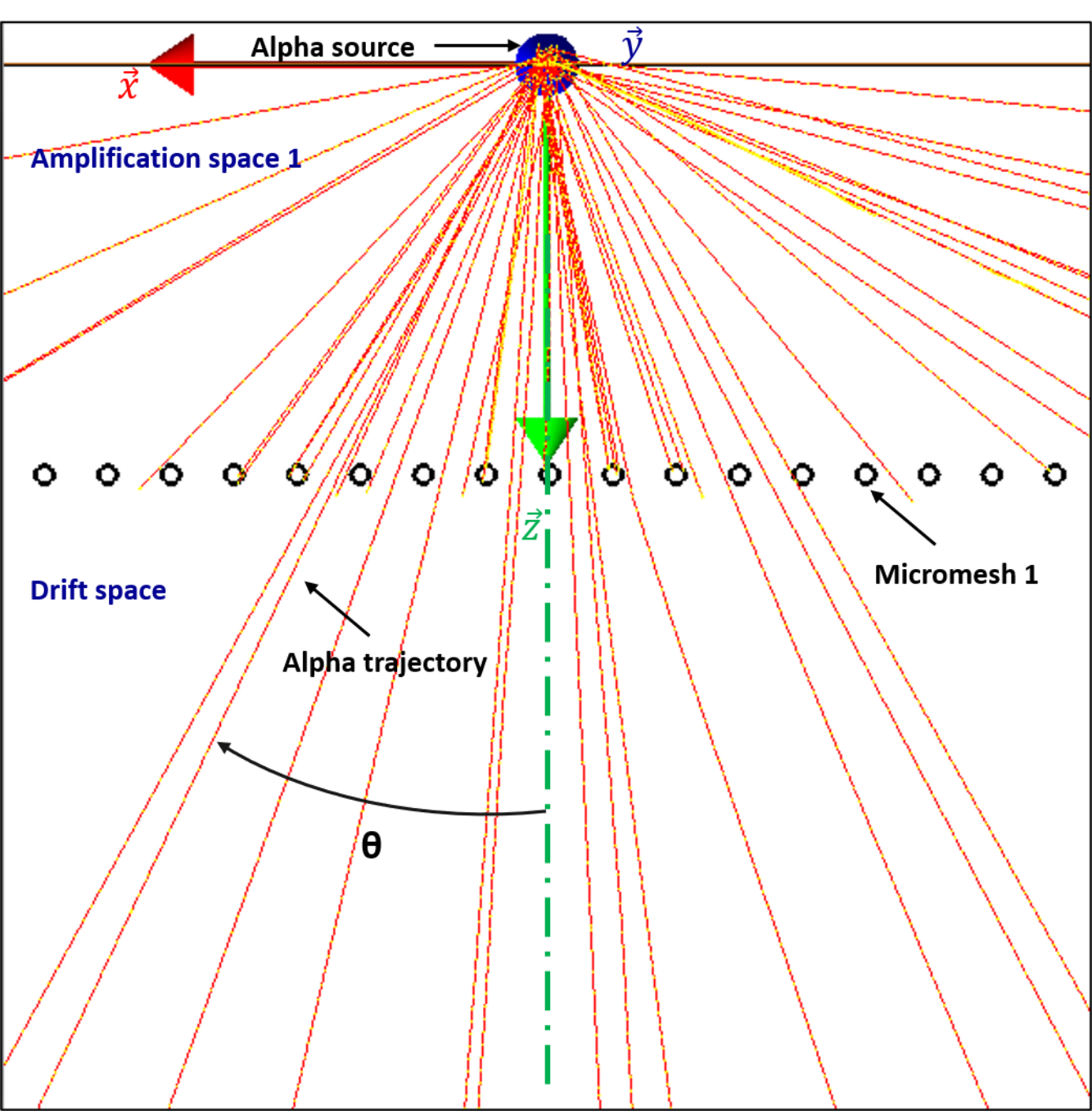
Figure 14: Difference between spectrum 1 (spectroscopy chain alpha spectrum distribution after degradation) and spectrum 2 (PIM detector spectrum depending of G_2) distributions for ^{226}Ra source, function of gain G_2 .

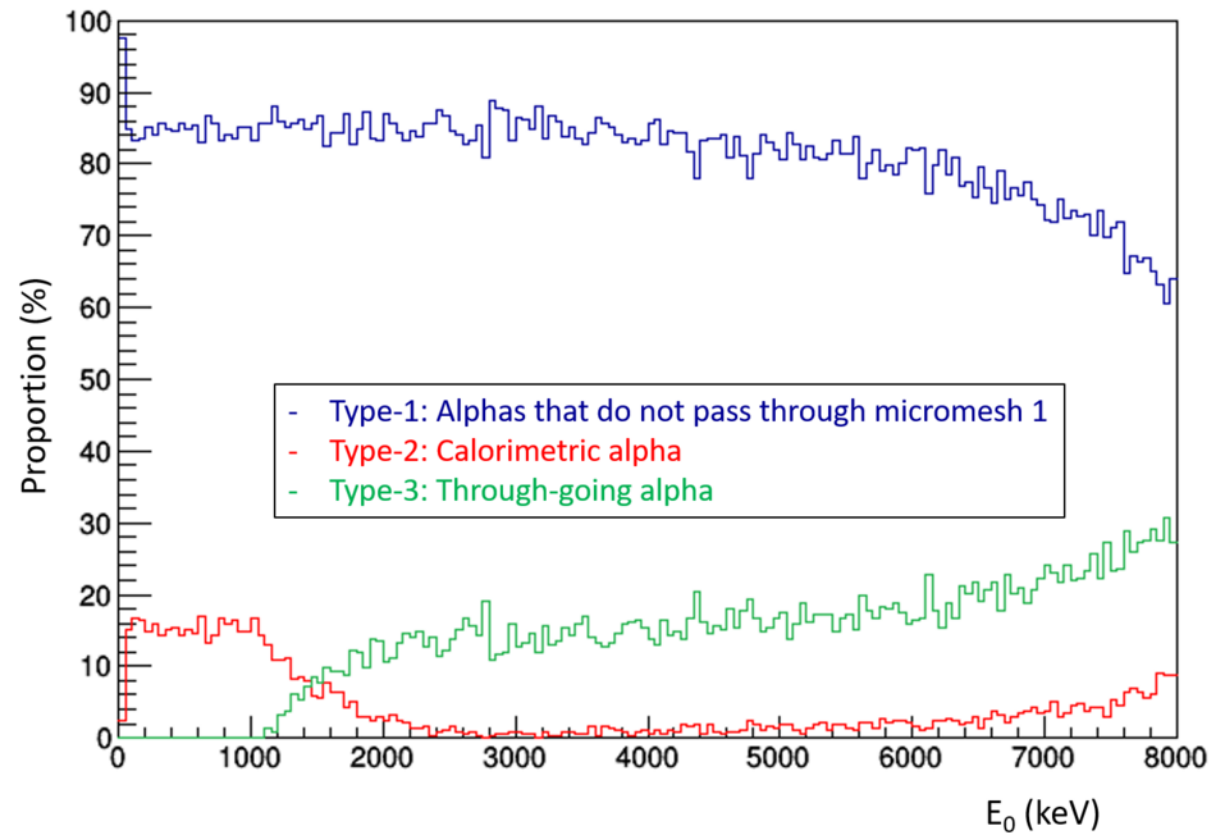
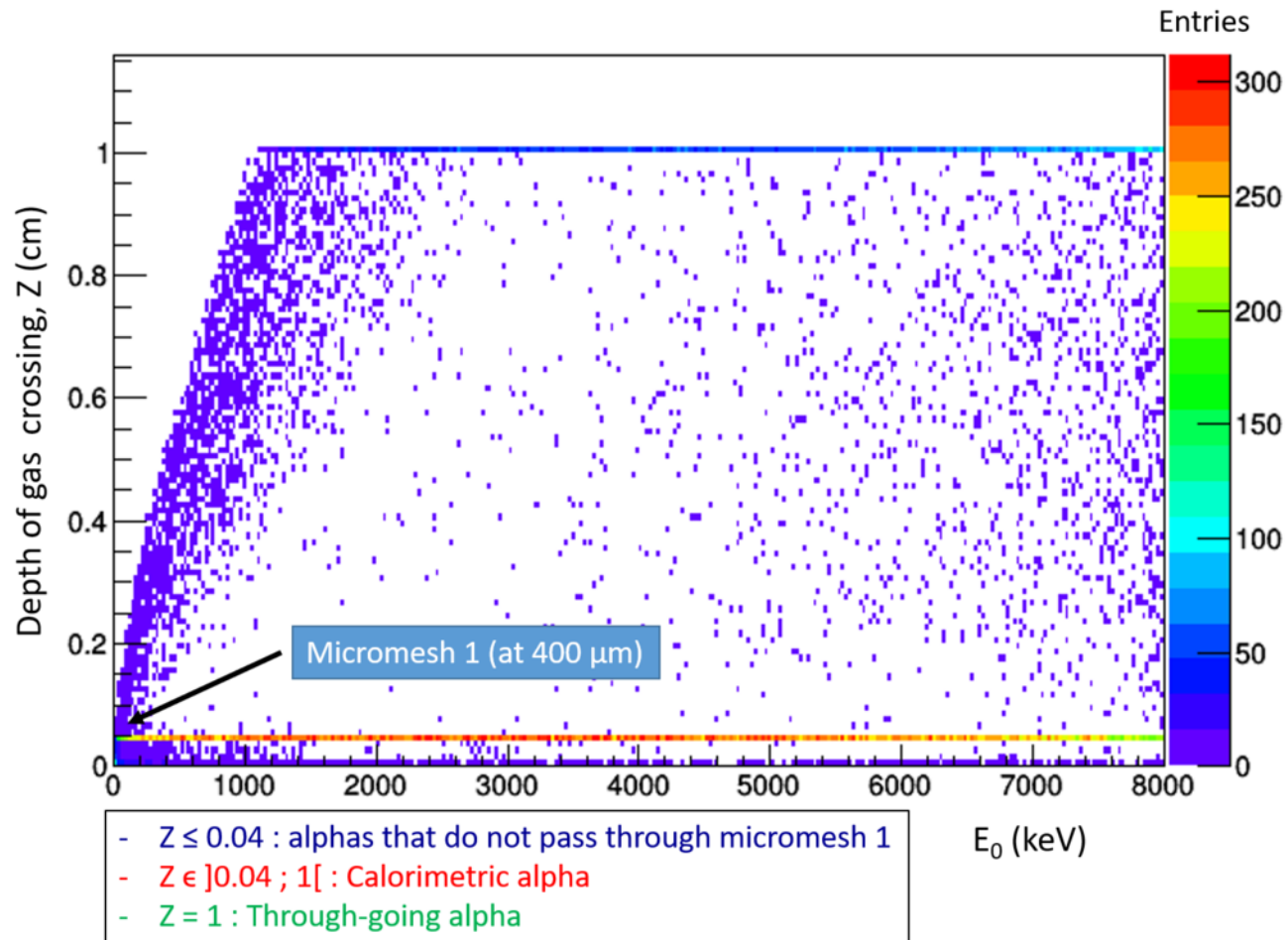
Figure 15: Energy spectrum of uranium ore sample measured by alpha spectrometry. There are 8 alpha emitters from the ^{238}U decay product: ^{238}U , ^{234}U , ^{230}Th , ^{226}Ra , ^{222}Rn , ^{218}Po , ^{214}Po and ^{210}Po .

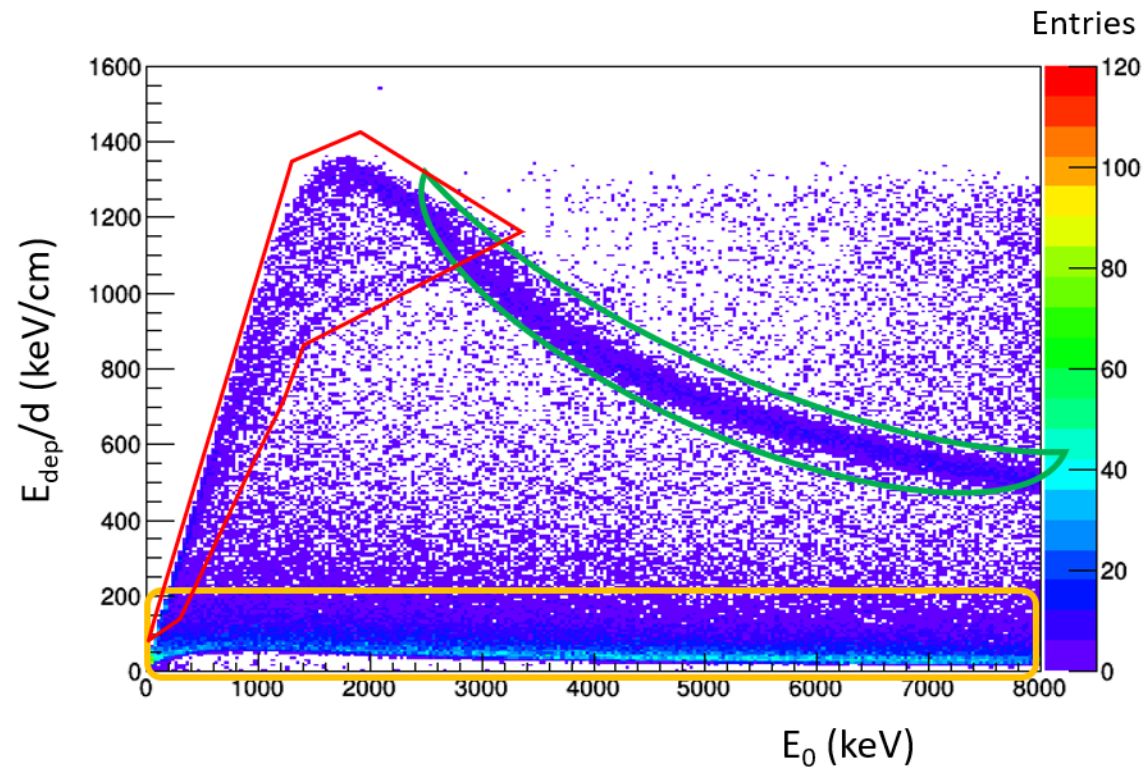
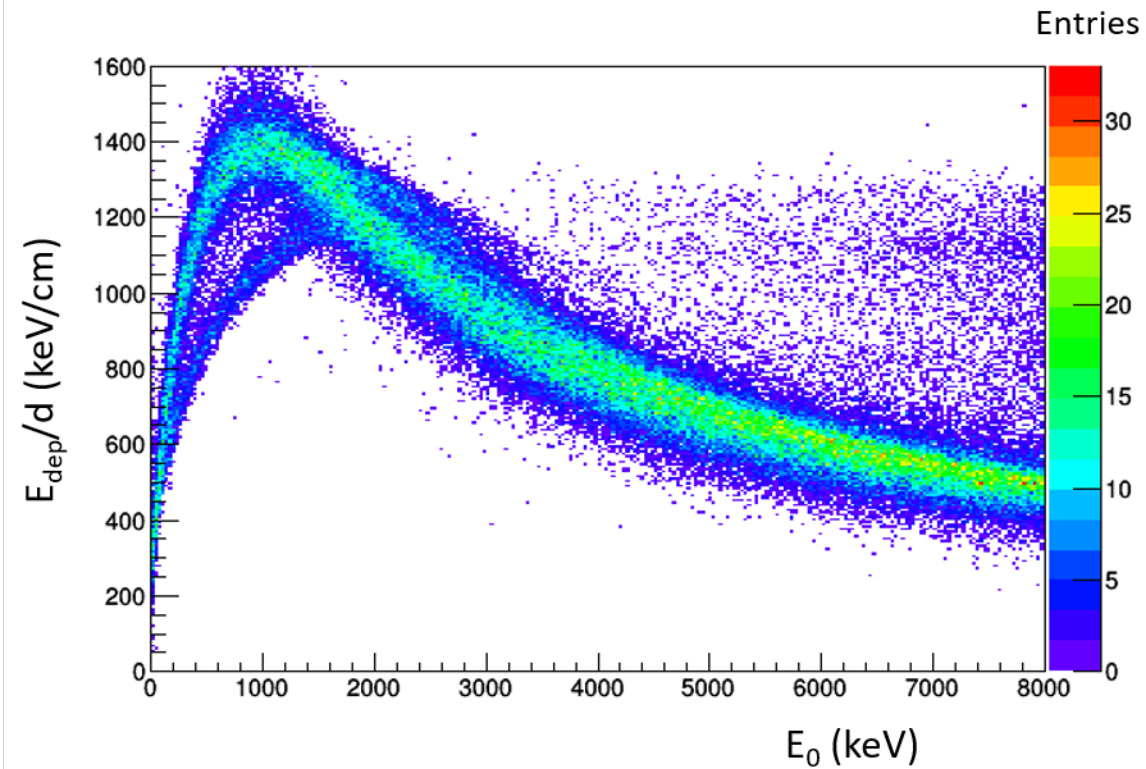
Figure 16: Picture (left) of the uranium ore sample from the Congo (in the form of a “piece”) and the corresponding alpha autoradiograph (right).

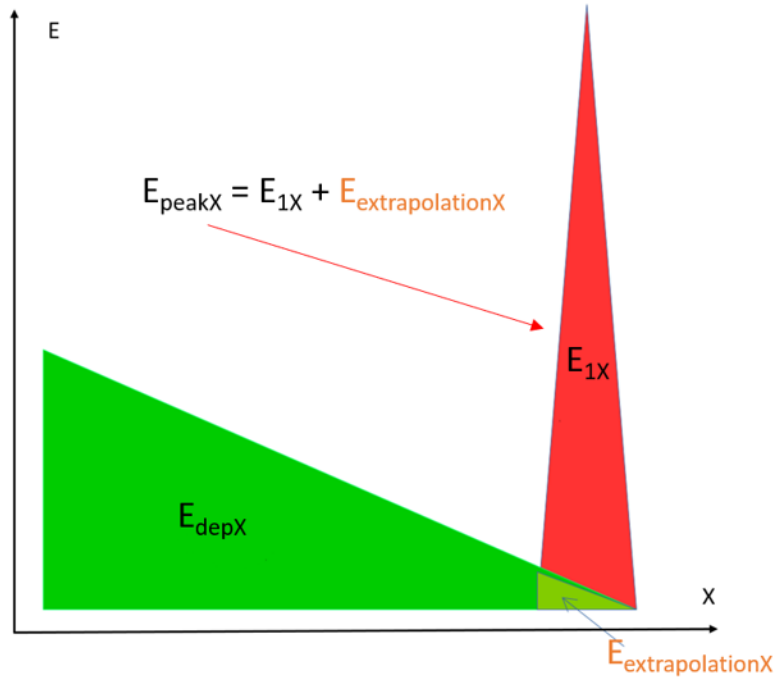
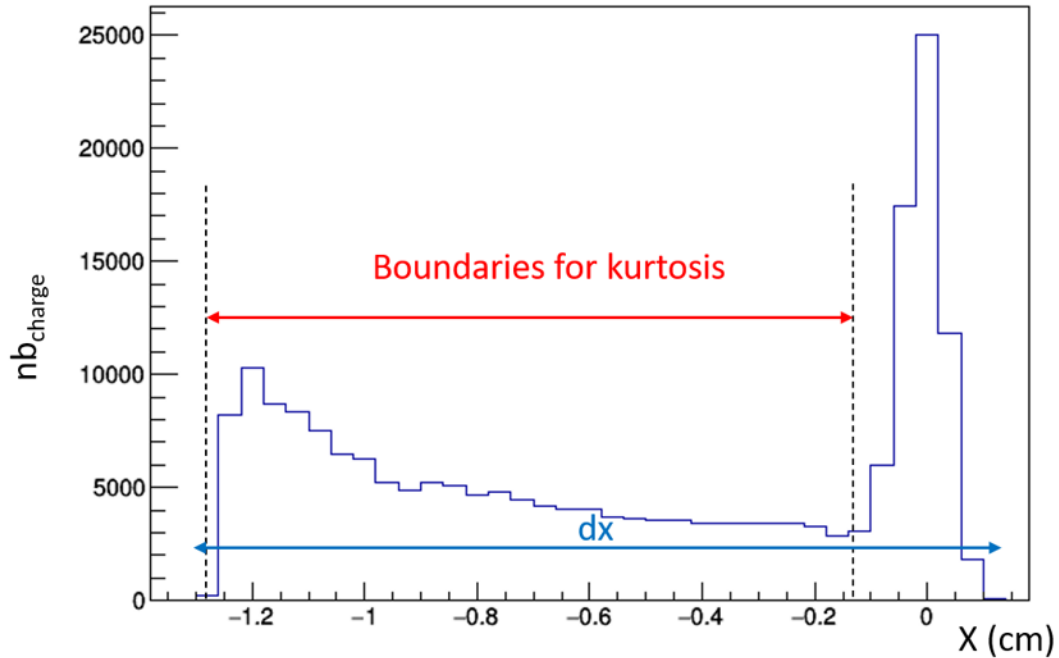
Figure 17: Comparison of the spectrum (divided by its respective internal) of uranium ore obtained with the PIM detector and SA method (in red) with the spectrum obtained from the spectrometry chain after degradation (in blue).

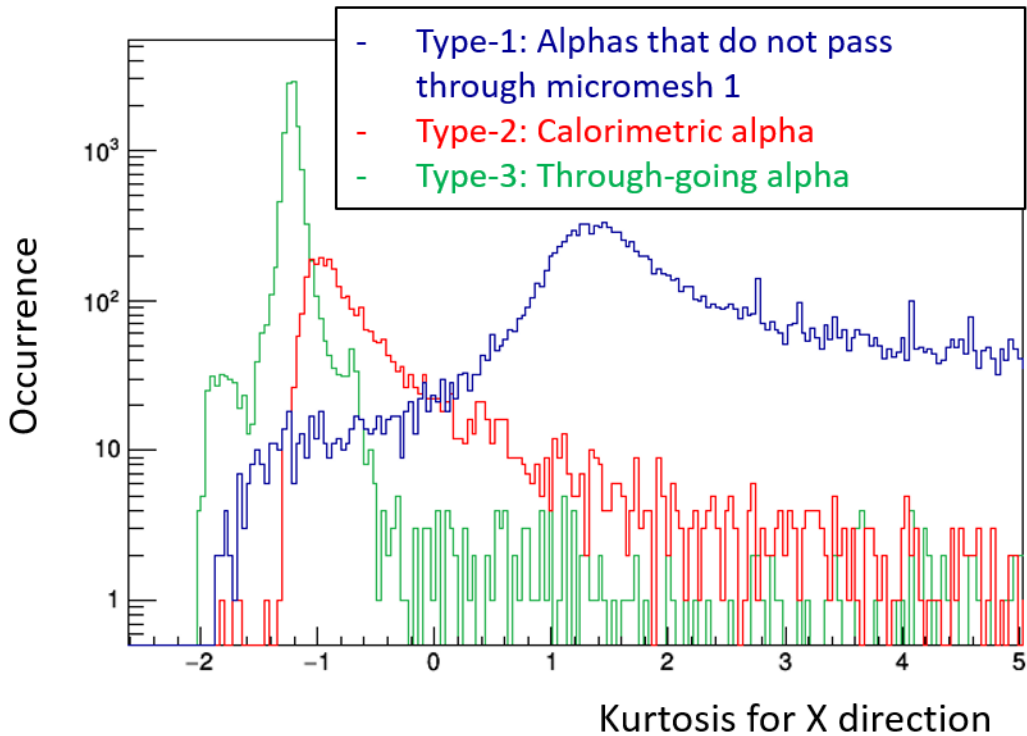


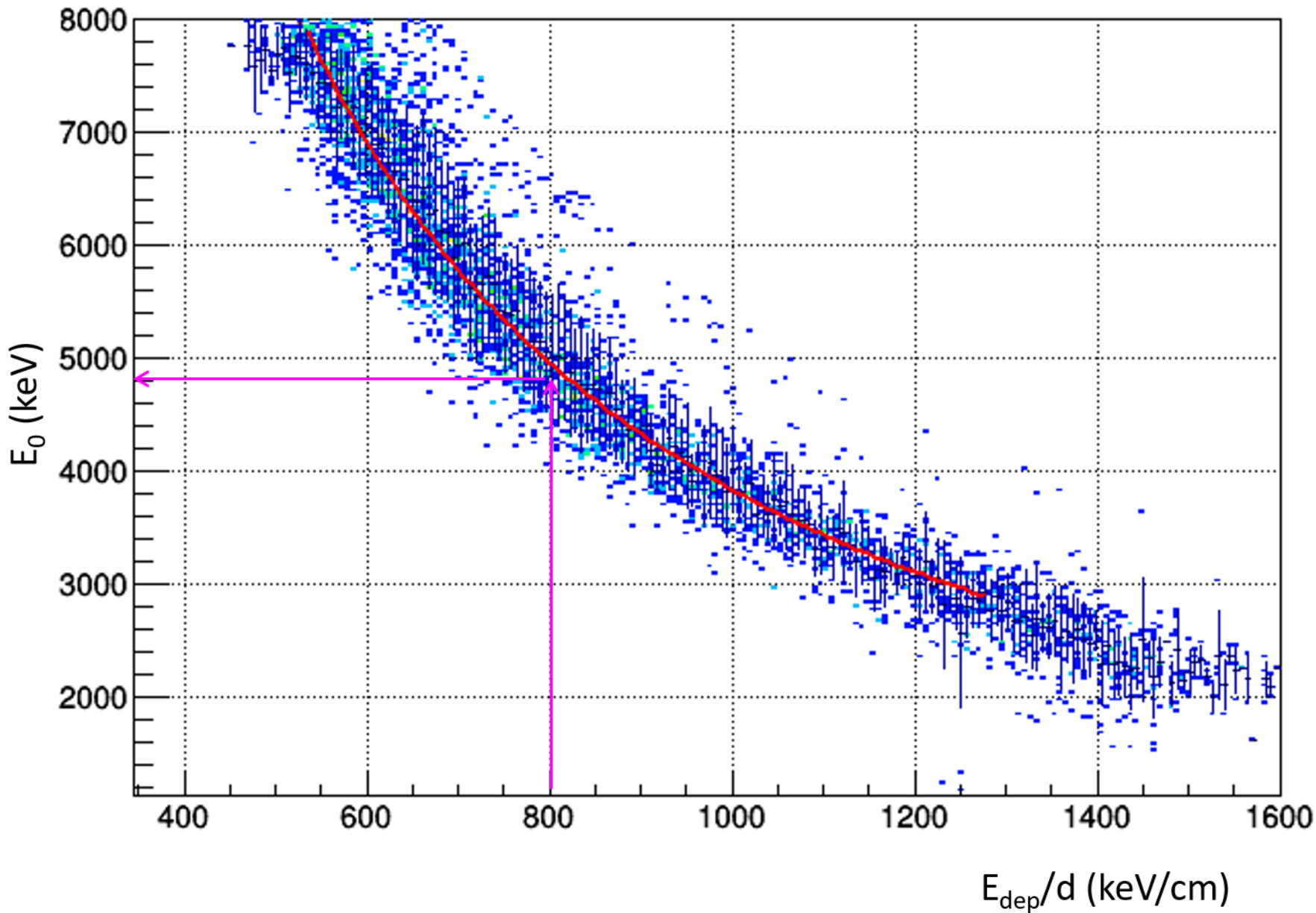


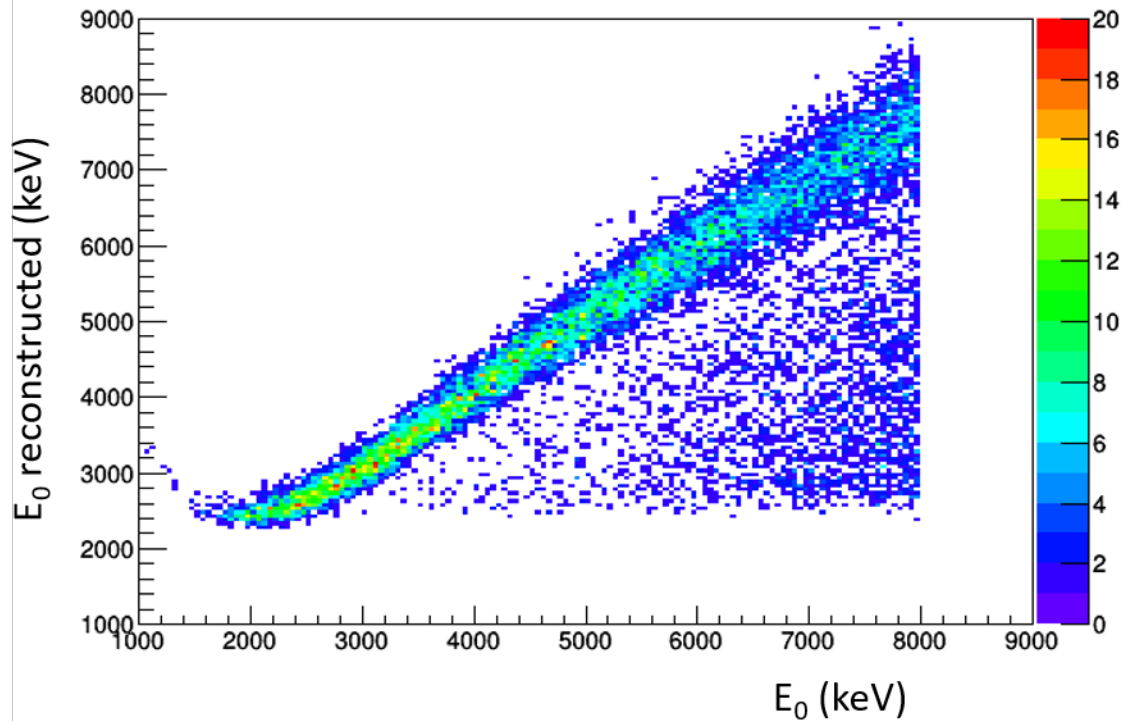


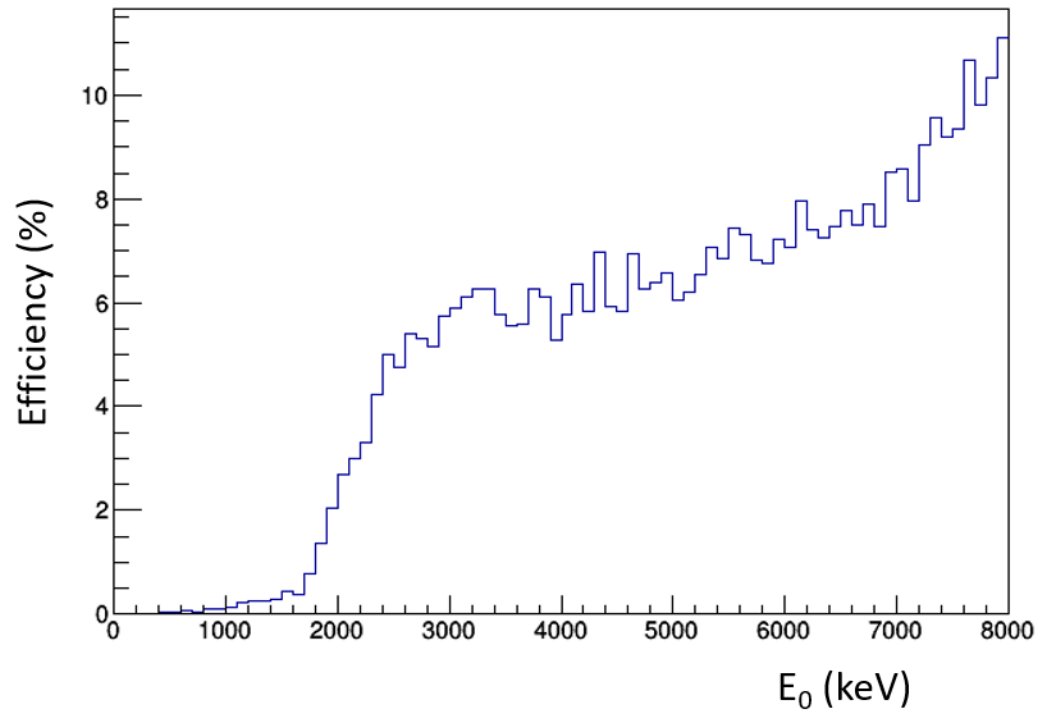
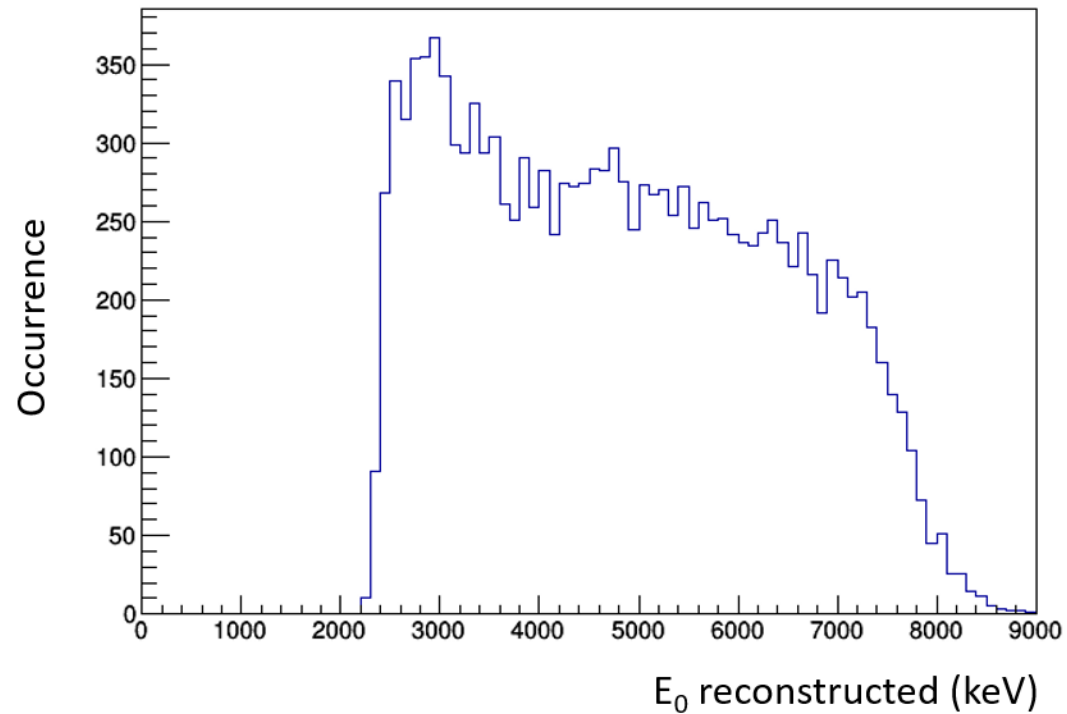


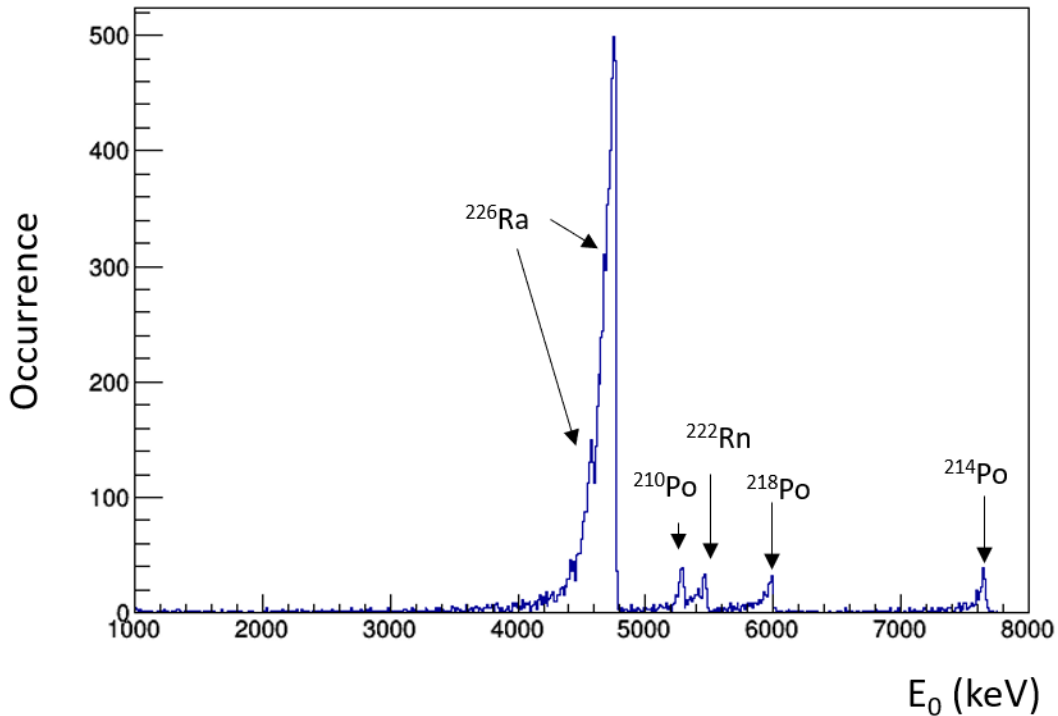


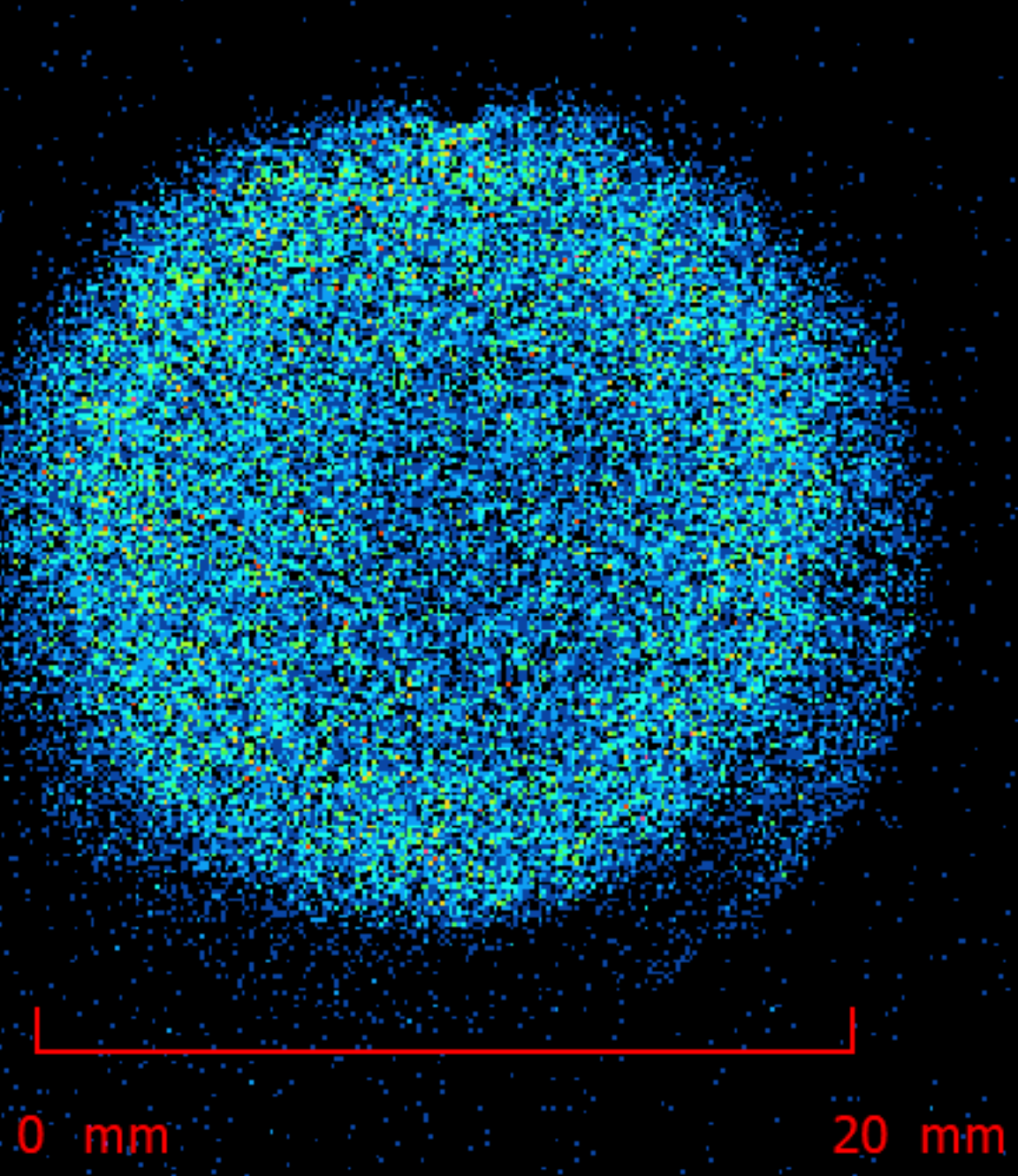




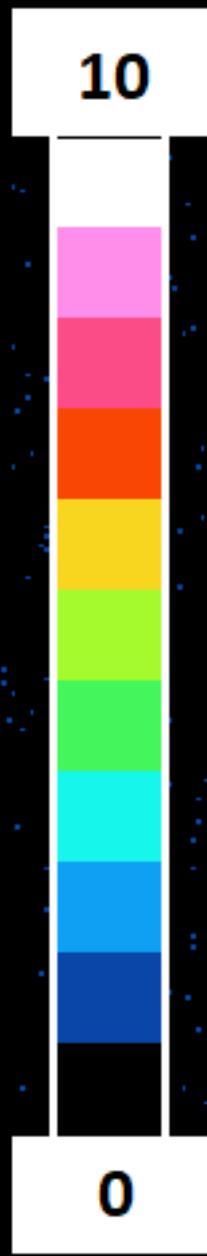


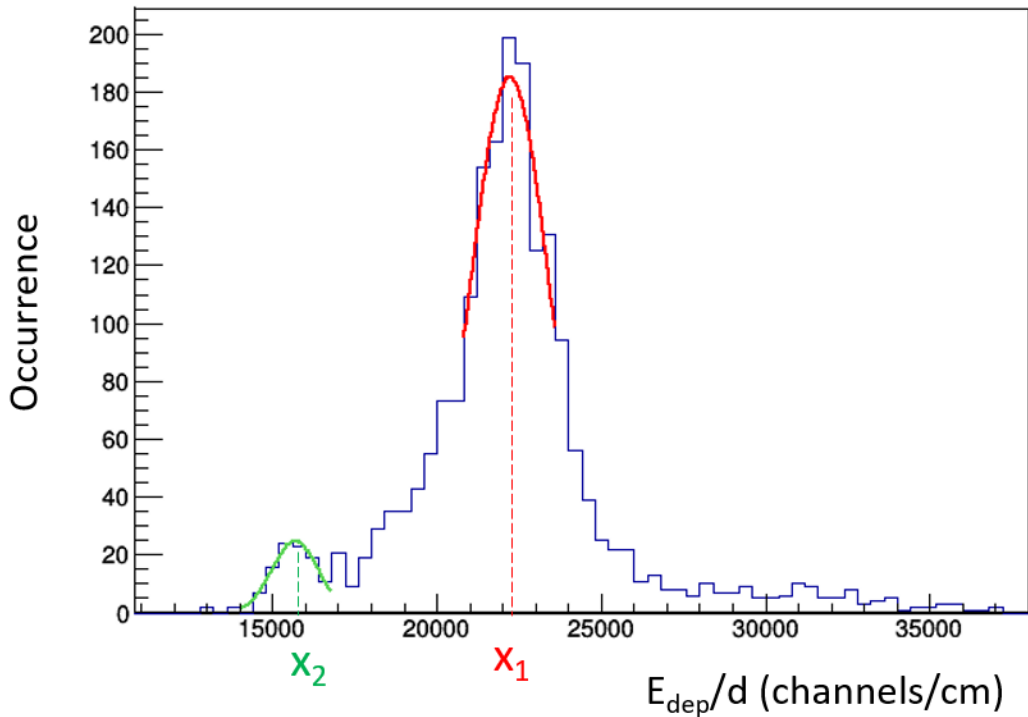


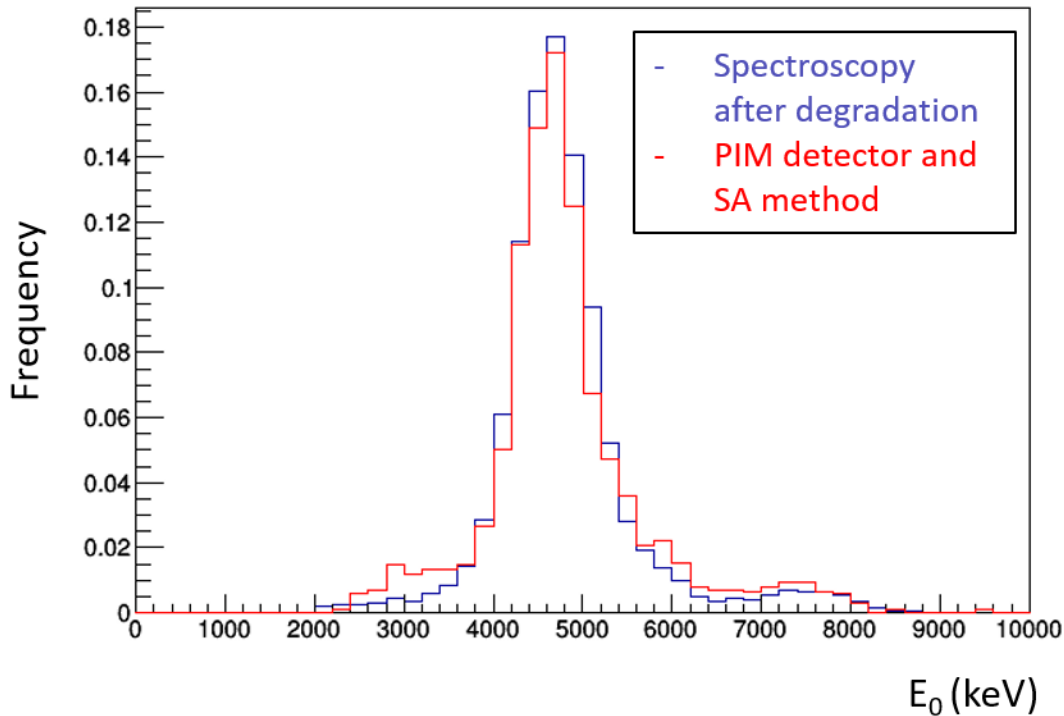


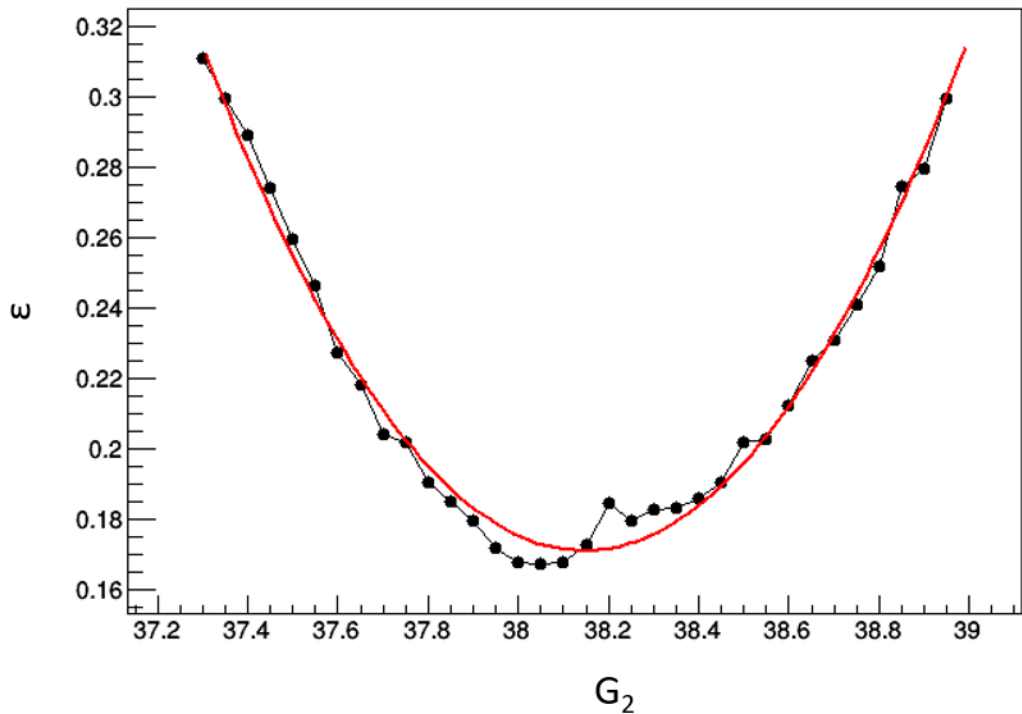


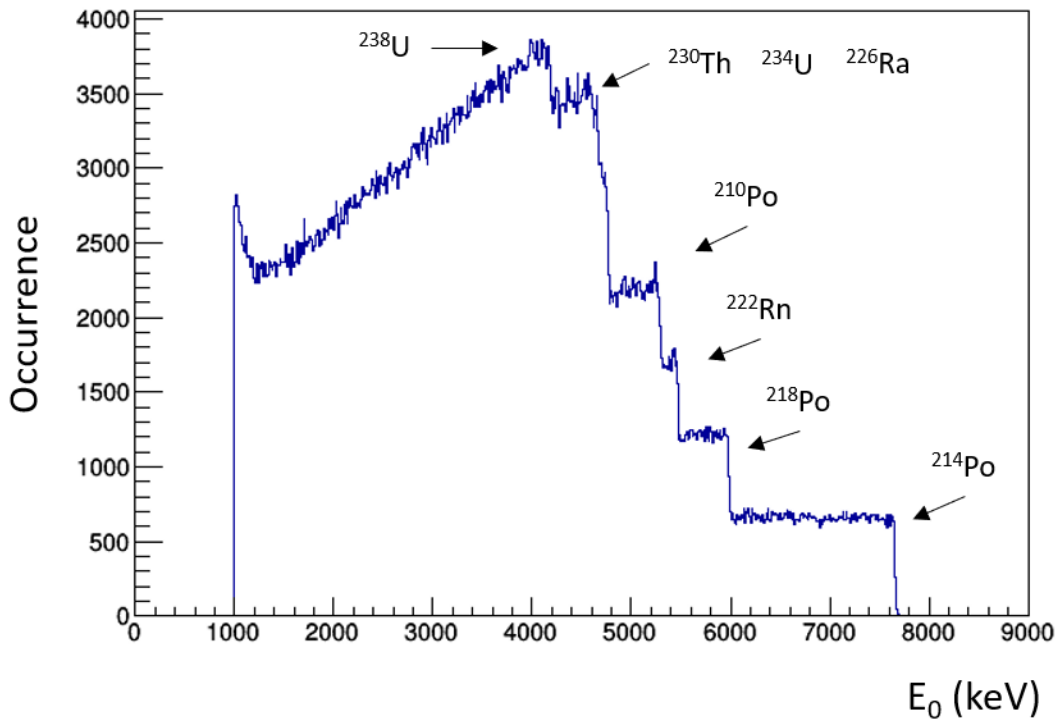
Counts

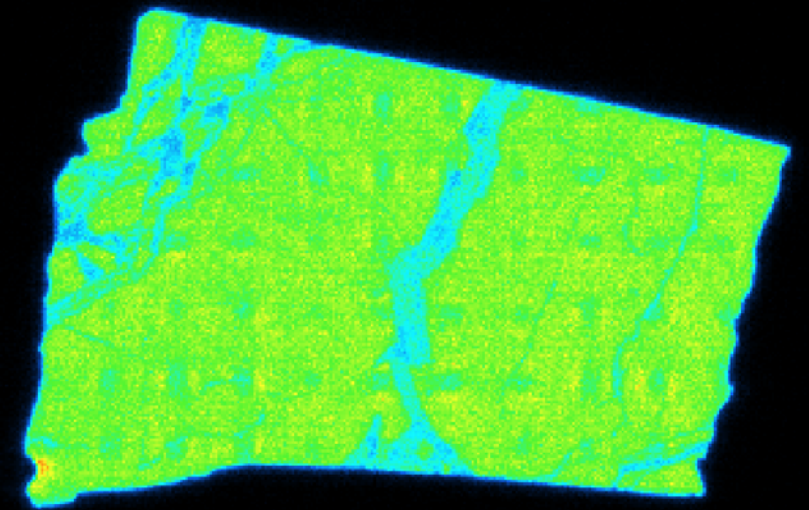
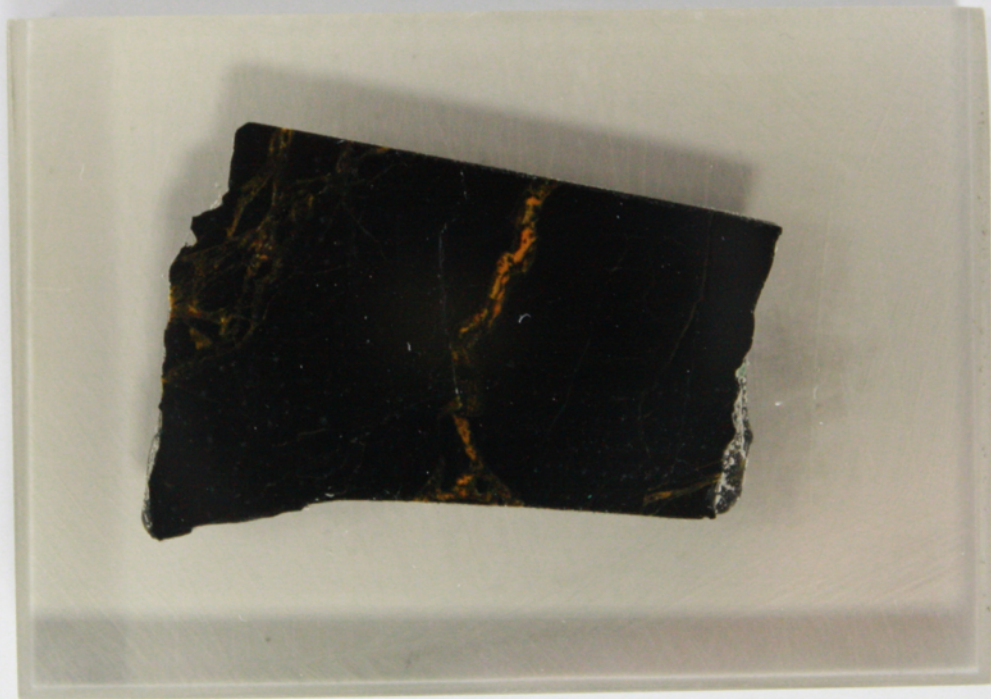












0 mm

25 mm

Counts

700

0

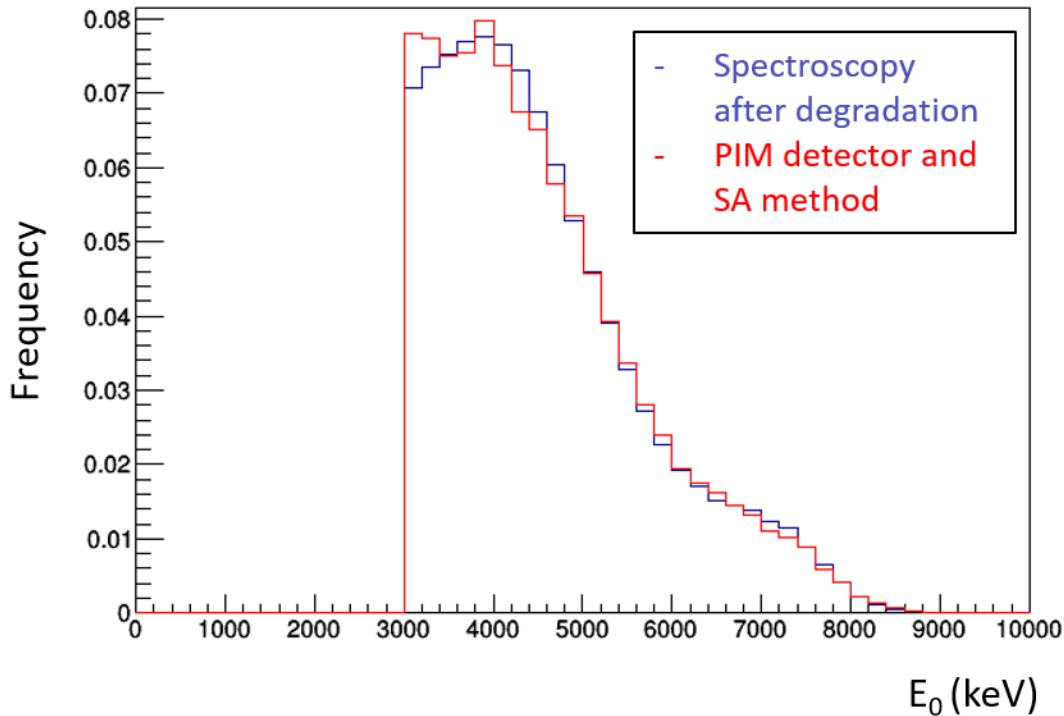


Table 1: Comparative table of important parameters describing the spectroscopic autoradiography devices. These parameters are related to alpha particles detection.

Detector	Sensitive Material technology	Energy Resolution (FWHM)	Spatial Resolution	Active Area	Reference(s)
SiPM	Ce:GAGG Scintillator	13% (5.5 MeV)	600 μm	26x26 mm^2	[32]
PSPMT	Stilbene	21.6% (5.5 MeV)	-	20x20 mm^2	[33]
CCD Camera	ZnS(Ag)	56.4 % (5.5 MeV)	390 μm	26x26 mm^2	[45]
Timepix	Silicon semi-conductor	0.73% (5.5 MeV)	18 μm	14x14 mm^2	[36] [37]
SSNTD	Lexan polycarbonate	6.9% (5.2 MeV)	Several micrometers		[29] [30]
FNTD	$\text{Al}_2\text{O}_3\text{:C,Mg}$ crystals	11.8% (5.49 MeV)	-	70x70 μm^2	[41]
Micro-TPC	Gas: CF_4	15.8% (5.3 MeV)	6.8 mm	95x95 mm^2	[44]
Coplanar electrode	Gas: Xe + 0.7% CH_4	1.3% (5.49 MeV)	No position	100 mm	[42]
Coplanar electrode	Gas: Ar + 10% CH_4	2.2% (5.49 MeV)	No position	-	[43]